

Chapter 2

Background

Nuclear physics deals with the study of the fundamental properties of nuclear matter and the character of the strong nuclear force. By the 1960s the concept of nuclear matter had been extended from the nucleons making up atomic nuclei to a vast number of strongly interacting particles known as hadrons. The flavor symmetries among various types of hadrons suggested that these particles are composite particles with their quantum numbers carried by common, sub-hadronic objects, and that these objects possessed a new quantum number known as color [1]. A group theoretic approach to hadron taxonomy led to the development of the Quark Model [2–6] which predicted the Ω^- baryon observed at BNL in 1964 [7].

Developments in current algebra led to a proposed scaling behavior of the structure functions in deep inelastic scattering. Bjorken Scaling [8] implies that at high momentum transfer, Q^2 , the hadronic structure functions are independent of Q^2 and functions of a single scaling variable, x . Scaling behavior consistent with this relation was observed in a series of measurements in deep inelastic scattering (DIS) at SLAC [9, 10], leading to the interpretation of point-like constituents within the nucleon known as the Parton Model [11–13].

Advances in renormalization group techniques [14–17] led to the conclusion that only a theory possessing asymptotic freedom, a coupling strength that becomes arbitrarily weak at high energies, could be consistent Bjorken Scaling [18, 19]. The symmetry considerations of the Quark Model suggested that non-Abelian gauge theories [20] would be potential candidates for such a theory. These theories were found to possess the required renormalization criteria with the β -function in the calculation of the running of the coupling being negative for an SU(3) gauge symmetry [21, 22]. Furthermore, explicit calculations of the anomalous dimensions of the DIS structure functions showed that these non-Abelian gauge theories possessed scaling properties consistent with experimental observations [23–26].

This description of the strong interaction as an SU(3) (color) gauge symmetry between spin- $\frac{1}{2}$ quarks and mediated by massless spin-1 gluons is known as Quantum Chromodynamics (QCD). At short distance scales, asymptotic freedom ensures that the coupling becomes weak and perturbative techniques can be used to calculate observables. The validity of QCD as the correct theory of the strong interaction

has been rigorously demonstrated by a variety of experimental results that are well described by perturbative calculations. A summary of this evidence is presented in Sect. 2.1.

Color charges are never observed as isolated particles but rather as constituents of color neutral hadrons, an aspect of QCD known as confinement. Furthermore, the QCD Lagrangian possess chiral symmetry which is dynamically broken through the interactions that bind the quarks into hadrons and is responsible for the vast majority of the mass of ordinary matter.¹ However, at soft momentum scales the coupling becomes increasingly large and at hadronic energies the theory is non-perturbative. This leads to significant challenges in theoretical calculations and interpreting experimental results, and much of the work done since the inception of QCD has been to navigate these challenges to develop a comprehensive picture of the strong interaction.

2.1 Experimental Evidence for QCD

Initial experimental evidence for QCD as a theory of the strong interaction was provided in DIS through the observation of Bjorken Scaling. Measurements of the proton structure function F_2 are shown in Fig. 2.1, and DIS structure functions in the context of the Parton Model and collinear factorization are further discussed in Sect. 2.3. Subsequent tests of the theory have been performed in e^+e^- collisions and hadronic collisions, particularly through the Drell-Yan process, the inclusive production of lepton pairs in hadronic scatterings, $A + B \rightarrow l^+l^- + X$ [27]. These results have provided overwhelming experimental support for QCD [28, 29], and a brief survey is discussed below.

The Callan-Gross [30] relation between the DIS structure functions, $2xF_1 = F_2$, arises due to scattering off spin- $\frac{1}{2}$, point-like objects; the measured behavior of the structure function, shown in Fig. 2.2, is approximately consistent with this relation. In e^+e^- collisions the ratio of cross sections for the production of inclusive hadrons to muon pairs is given to leading order in QCD by

$$R(s) = \frac{\sigma(e^+e^- \rightarrow \text{hadrons}, s)}{\sigma(e^+e^- \rightarrow \mu^+\mu^-, s)} = N_c \sum_f^{N_q} Q_f^2, \quad (2.1)$$

where s is the center of mass energy, N_c is the number of colors ($N_c = 3$ for QCD), and Q_f is the charge of quark f . The sum runs over the quark flavors up to the heaviest quark capable of being produced at that s . This ratio, aside from resonance peaks and away from the Z threshold, is measured to be approximately constant with discrete jumps at the quark mass thresholds as shown in Fig. 2.3.

¹ This symmetry is only approximate as it is broken explicitly by the quark masses. Thus the pions are pseudo-Goldstone bosons.

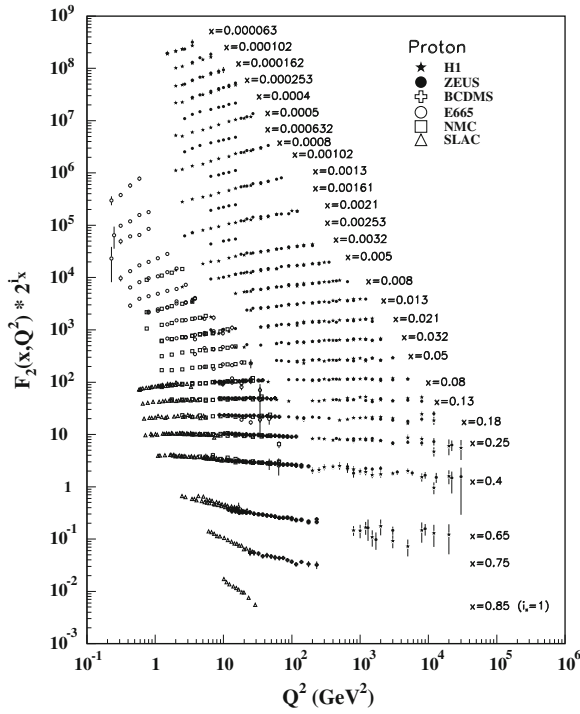


Fig. 2.1 The proton structure function F_2 versus Q^2 at fixed x measured by a variety of experiments (see [29] and references therein). F_2 is approximately independent of Q^2 . The observed logarithmic violations of this scaling are well-described by the QCD phenomenon of parton evolution

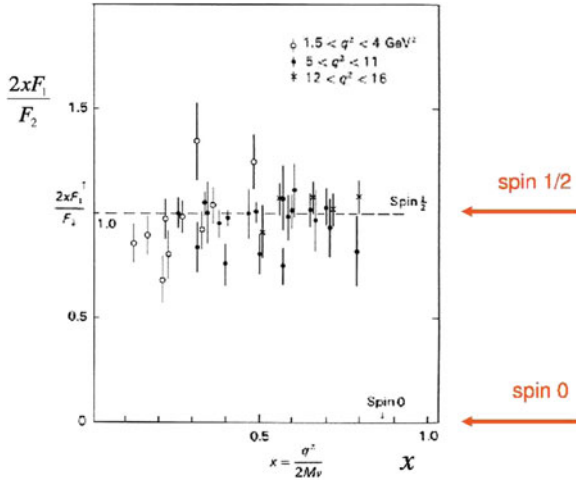


Fig. 2.2 The ratio $2xF_1/F_2$ as a function of x [31]. The ratio is approximately independent of x , consistent with the Callan-Gross relation, which is the result of scattering off of spin- $\frac{1}{2}$ constituents within the proton

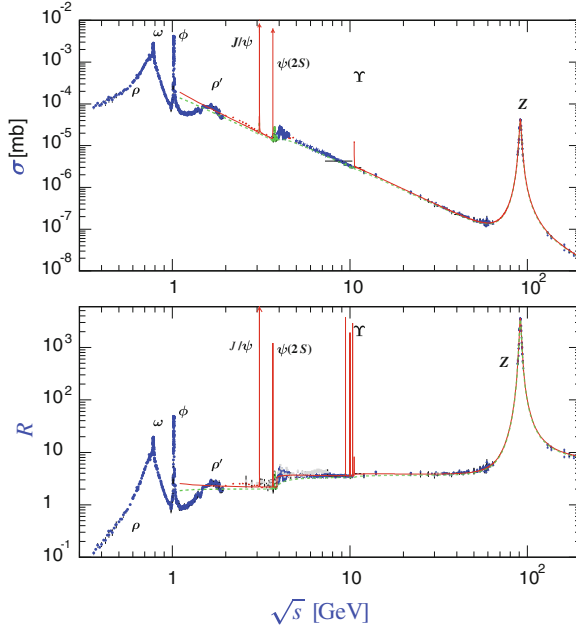


Fig. 2.3 World data on inclusive $e^+e^- \rightarrow \text{hadrons}$ cross section (top) and ratio to muon pair production cross sections (bottom) [29, 32]

Highly collimated, energetic sprays of particles balanced in momentum known as jets were observed in e^+e^- collisions at SLAC [33], consistent with the hypothesis that hadrons are produced in these collisions through the production of $q\bar{q}$ pairs of opposite momentum. The observation of three jet events at PETRA through the process $e^+e^- \rightarrow q\bar{q}g$ provided experimental evidence for the gluon as well as measurements of the strong coupling constant α_s [34]. Further precision measurements of the strong coupling constant have shown remarkable consistency [35] and a summary is shown in Fig. 2.4.

2.2 Fundamentals of QCD

QCD is the quantum field theory that describes the strong nuclear force, and is expressed in terms of quarks and gluons which contain color charge described by an SU(3) gauge symmetry. The spin- $\frac{1}{2}$ quarks fields, ψ_a , transform under the fundamental, three-dimensional, representation of the gauge group,

$$\psi'_a(x) = e^{i\alpha^C(x)t^C_{ab}}\psi_b(x) = U_{ab}(x)\psi_b(x), \quad (2.2)$$

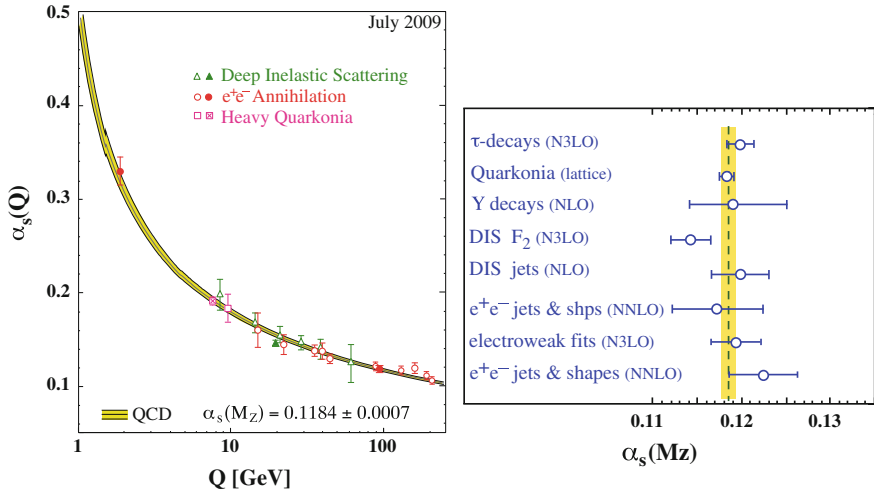


Fig. 2.4 The strong coupling constant, α_s , as a function of Q^2 (left) and fixed at $Q^2 = m_Z^2$ (right). Figure adapted from Ref. [35]. From these results, α_s was determined to have a world average of $\alpha_s(m_Z) = 0.1184 \pm 0.0007$

with the subscript a describing the quark color. The t_{ab}^C are the generators of the gauge group, represented by eight 3×3 matrices ($C = 1, \dots, 8$, $a, b = 1, 2, 3$), and obey the Lie Algebra²

$$[t^A, t^B] = f^{ABC} t^C, \quad (2.3)$$

with f^{ABC} the structure constants of $SU(3)$. The local gauge symmetry is imposed by replacing the derivatives appearing in the usual Dirac Lagrangian with the gauge-covariant derivative, $D_{\mu,ab}$,

$$D_{\mu,ab} = \partial_\mu \delta_{ab} + ig A_\mu^C t_{ab}^C. \quad (2.4)$$

The color indices a and b on D are explicit here to indicate that the covariant derivative is Lie Algebra-valued (i.e. matrix-valued). The covariant derivative introduces a non-Abelian coupling, of strength g , between the quarks and massless, spin-1 gauge fields A_μ^C representing gluons. These transform under the adjoint, eight-dimensional, representation of the gauge group. Including the pure Yang-Mills action for the gauge fields, the full QCD Lagrangian is given by

$$\mathcal{L} = \sum_q \bar{\psi}_q (i \gamma^\mu D_\mu - m_q) \psi_q - \frac{1}{4} F_{\mu\nu}^A F^{A\mu\nu}, \quad (2.5)$$

² In this section the generator/adjoint indices are denoted by capital, Roman script, as a superscript with the summation over repeated indices is implied. The fundamental, matrix multiplication indices are denoted by lower case, Roman script appearing as subscripts. The Lorentz indices are indicated by Greek characters and the standard Einstein summation convention applies.

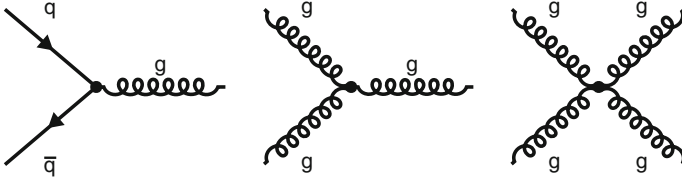


Fig. 2.5 Possible couplings allowed by the QCD Lagrangian. The quark-gluon (*left*) and three-gluon (*center*) vertices are proportional to g . The four-gluon vertex is proportional to g^2

with the index q denoting the quark flavor with mass m_q . The field strength tensor $F_{\mu\nu}^A$ is expressed in terms of the gauge field via

$$F_{\mu\nu}^A = \partial_\mu A_\nu^A - \partial_\nu A_\mu^A - gf^{ABC}A_\mu^B A_\nu^C. \quad (2.6)$$

The QCD vertices are shown in Fig. 2.5. In addition to the analog of the QED gauge coupling shown on the left, the non-Abelian structure of the theory allows for coupling between the gauge fields themselves. Color factors, associated with different processes, arise from the group structure in the Feynman rules,

$$t_{cd}^A t_{cd}^B = T_F \delta^{AB}, \quad f^{ACD} f^{BCD} = C_A \delta^{AB}, \quad t_{bc}^A t_{cd}^A = C_F \delta_{bd}. \quad (2.7)$$

In QCD, these have values

$$T_F = \frac{1}{2}, \quad C_A = 3, \quad C_F = 4/3, \quad (2.8)$$

and are typically associated with the splittings $g \rightarrow q\bar{q}$, $g \rightarrow gg$ and $q \rightarrow qg$ respectively.

The quantization of this theory is typically performed using the path integral formalism. In this technique, the gauge-fixing condition imposes a constraint on the functional integral which can be removed by the introduction of Faddeev-Popov ghost fields [36]. These unphysical fields appear as an artificial mechanism for preserving gauge invariance. Their contributions, and the contribution of the gluon propagator, will depend on the choice of gauge, with this dependence dropping out in the computation of any gauge invariant quantity.

2.2.1 Ultraviolet Behavior

The ultraviolet (UV) behavior of QCD was the main reason it was originally proposed as the theory of the strong interaction. The relationship among the UV divergences is

encoded in the Callan-Symanzik equation. In particular, the derivative of the coupling constant with respect to the renormalization scale, μ , is defined by the β -function,

$$\frac{\partial g}{\partial \ln \mu} = \beta(\mu). \quad (2.9)$$

The one-loop β -function for $SU(N)$ non-Abelian gauge theories was first computed by Politzer [21], Gross and Wilczek [22] in 1973. For $N = 3$ it is given by

$$\beta(\alpha_S) = -g \left(\frac{\alpha_S}{4\pi} \beta_1 + \left(\frac{\alpha_S}{4\pi} \right)^2 \beta_2 + \dots \right), \quad (2.10)$$

with $\alpha_S = g^2/4\pi$. The one and two-loop coefficients are

$$\beta_1 = 11 - \frac{2}{3}N_f, \quad \beta_2 = 102 - \frac{38}{3}N_f. \quad (2.11)$$

To one-loop, the solution is

$$\alpha_S(\mu) = \frac{\alpha_S(\mu_0^2)}{1 + \frac{\beta_1}{4\pi} \alpha_S(\mu_0^2) \ln(\mu^2/\mu_0^2)} = \frac{4\pi}{\beta_1 \ln(\mu^2/\Lambda_{\text{QCD}}^2)} \quad (2.12)$$

$$\Lambda_{\text{QCD}} = \mu_0 e^{-2\pi/(\beta_1 \alpha_S(\mu_0^2))},$$

where Λ_{QCD} is used to set the scale of the strong coupling. To higher order in $\ln \mu^2/\Lambda$ this is

$$\alpha_S(\mu) = \frac{4\pi}{\beta_1 \ln(\mu^2/\Lambda^2)} - \frac{\beta_2 \ln[\ln(\mu^2/\Lambda^2)]}{\beta_1^3 \ln^2(\mu^2/\Lambda^2)} + \mathcal{O}\left(\frac{1}{\beta_1^3 \ln^2(\mu^2/\Lambda^2)}\right), \quad (2.13)$$

where the definition of Λ becomes dependent on the renormalization scheme. The result above is for the $\overline{\text{MS}}$ scheme [28]. As the renormalization scale is increased the coupling decreases, as indicated by the leading $-$ sign in the β -function. This property is asymptotic freedom. For general $SU(N)$, $\beta_1 = \frac{1}{3}(11N_c - 2N_f)$. The leading, positive term is due to the gluons, which reduce the coupling at large μ . There is competition, which weakens the asymptotic freedom, from the second term which is due to fermion loops and is proportional to the number of flavors.

2.2.2 Infrared Behavior

Although QCD is well behaved at large momenta, the infrared behavior must be handled with care in perturbative calculations. Since gluons (and to a good approximation the light quarks) are massless, any sensitivity to the long range behavior of QCD appears in perturbation theory as an infrared divergence. Fortunately, the

configurations that introduce this sensitivity have been systematically analyzed and a formal procedure exists to define quantities which are infrared safe [37–39]. These divergences are associated with the contributions to the momentum integration where the massless particle has zero momentum (soft) or at zero angle (collinear). Observables that are safe from these divergences must be insensitive with respect to the emission of an additional soft or collinear gluon. Formally, this means that for an inclusive quantity \mathcal{I} , defined by the functions \mathcal{S}_n ,

$$\mathcal{I} = \frac{1}{2!} \int d\Omega_2 \frac{d\sigma_2}{d\Omega_2} \mathcal{S}_2(p_1^\mu, p_2^\mu) + \frac{1}{3!} \int d\Omega_3 \frac{d\sigma_3}{d\Omega_3} \mathcal{S}_3(p_1^\mu, p_2^\mu, p_3^\mu) + \cdots, \quad (2.14)$$

the quantity is said to be infrared and collinear (IRC) safe if

$$\mathcal{S}_{n+1}(p_1^\mu, p_2^\mu, \dots, (1-\lambda)p_n^\mu, \lambda p_{n+1}^\mu) = \mathcal{S}_n(p_1^\mu, p_2^\mu, \dots, p_n^\mu). \quad (2.15)$$

This idea is expanded in the discussion of applications of perturbative QCD in the following section.

2.2.3 Non-Perturbative Dynamics

Inspired by Wilson’s picture of renormalization, a discrete lattice formulation of QCD was developed to supplement perturbation theory where the latter is inapplicable [40]. This procedure uses the path integral formalism in Euclidean space-time, where the field configurations are explicitly integrated over. The integration is accomplished by recasting the quantity of interest in terms of gauge links between adjacent lattice sites. The finite lattice spacing, a , serves as an ultraviolet cutoff, and a valid lattice formulation must respect all of the features of QCD in the limit $a \rightarrow 0$. Technical challenges arise as spurious fermion states can be produced in this limit as lattice artifacts [41, 42]. This can be mitigated, although not completely removed, while maintaining chiral symmetry, by introducing staggered fermions [43]. Furthermore, the finite spacing introduces integration errors in the evaluation of the action. These can be minimized by using improved definitions of the action [44]. Advances in computing power and improved actions have led to highly accurate calculations, such as decay constants, form factors and the spectrum of hadrons, which is shown in Fig. 2.6. Additionally, the Euclidean path integral formulation is amenable to calculating thermodynamic quantities in QCD, a topic discussed in Sect. 2.4.2.

A qualitative picture of confinement is to view the static $q\bar{q}$ potential as Coulombic at short distances, but growing at long range,

$$V_{\text{QCD}}(r) = -\frac{4}{3} \frac{\alpha}{r} + kr. \quad (2.16)$$

A recent lattice calculation of the static quark potential is shown in Fig. 2.7, which indicates behavior approximately consistent with this analytic form. As

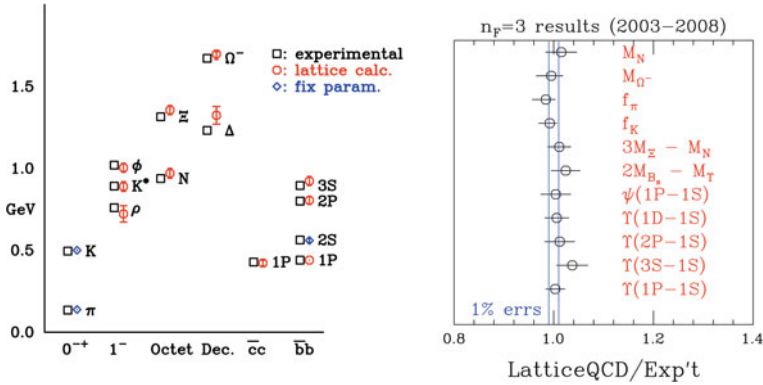


Fig. 2.6 Lattice calculation of the hadron spectrum with comparison to measured values (*left*) and ratios (*right*) [45]

the separation between the $q\bar{q}$ pair increases the force remains constant, and an increasing amount of energy is stored in the stretched gluon field called a flux tube. At some separation it becomes energetically favorable to break the flux tube and produce a new $q\bar{q}$ pair from the vacuum. This process, known as string fragmentation, is shown schematically in Fig. 2.8. Such a mechanism provides a heuristic construct for modeling confinement; no matter how much energy is applied only color-neutral objects can be created from the system. The flux tube picture has led to developments in hadron phenomenology by considering hadrons as relativistic strings [46, 47], and the constant, k , in Eq. 2.16 can be interpreted as a string tension. Monte Carlo (MC) event generators for simulating the production of hadrons have had a long history of success using string models [48, 49].

Fig. 2.7 Static quark potential as a function of r calculated with different values lattice spacings [45]. The distance is expressed in units of the lattice size, with the *colored gradations* indicating the scale in physical units

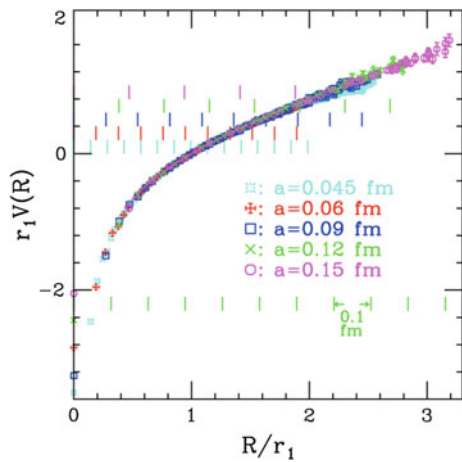




Fig. 2.8 Flux tube representing static $q\bar{q}$ potential (*left*) fragmenting into two color-neutral objects (*right*)

2.3 Applications of Perturbative QCD

2.3.1 The Parton Model and Factorization

QCD has had great success in providing reliable perturbative calculations of experimental observables. The most basic application of QCD uses the parton model, which is a tree-level, impulse approximation to the full perturbation theory. The scattering process is formulated in terms of point-like constituents integrated over probability distributions for a given parton to have momentum fraction x ,

$$\sigma_{AB}(p_A, p_B) \sim \sum_{i,j} \int dx_i dx_j \hat{\sigma}(x_i p_A, x_j p_B) \phi_i^A(x_i) \phi_j^B(x_j), \quad (2.17)$$

Here A and B denote the colliding hadrons and i and j denoting partons of a particular type. The functions $\phi_i^B(x_i)$ give the probability density of finding a parton of type i in hadron A with momentum $p_i = x_i p_A$. While asymptotic freedom ensures that at sufficiently hard scales the partonic level matrix elements are calculable in perturbation theory, almost any real world observable will involve hadronic initial and/or final-states, where the theory becomes non-perturbative. The applicability of Eq. 2.17 in certain kinematic regimes suggests that calculations can be performed by separating the short distance behavior of QCD, encoded in the partonic matrix element $\hat{\sigma}$, from the long range behavior represented by the probability distributions. The formal apparatus through which this is accomplished is known as factorization. Factorization theorems take a similar form to Eq. 2.17 where each term in the integrand is also dependent on a scheme-dependent factorization scale, μ_f . This parameter sets the cutoff for which aspects of the dynamics are being included in the description of the long and short range components. The form of the factorization ensures that there is no quantum mechanical interference between the long and short range behavior. Furthermore, the probability distributions, which are known as parton distribution functions (PDFs) in the general factorized formulation, are independent of the specific scattering process. Although they are not calculable by perturbation theory, once these functions are determined experimentally they can be applied to a calculation regardless of the details of the partonic level scattering, thus making them universal features of the hadrons. Factorization theorems have been proven for a variety of processes, $A + B \rightarrow C + D$ among particles A, B, C and D , with the schematic form of the theorem being

$$d\sigma(A + B \rightarrow C + D) = d\hat{\sigma} \otimes \Phi_A \otimes \Phi_B \otimes \Delta_C \otimes \Delta_D + \text{p.s.c.} \quad (2.18)$$

Here Φ and Δ denote the parton distribution and fragmentation functions (see Sect. 2.3.4) and \otimes represents a convolution over parton momentum fraction, trace over color indices and sum over parton species. This form is traditionally referred to as a twist expansion, with the first term known as the leading twist. The remainder terms, the power suppressed corrections, are suppressed by powers of a hard scale and are referred to as higher-twist effects. Most factorization theorems have been proven using a collinear factorization scheme, where the transverse momentum of the parton has been integrated over. These theorems have been proven in the cases of DIS and e^+e^- , but the only case involving hadron-hadron scattering to have been rigorously proven is the Drell-Yan process [50–52].

Observables such as spin asymmetries in hadronic collisions provide access to the spin structure of the proton. However, the extension of the usual collinear formalism in these cases has been problematic [53–56] as the observables contain sensitivity to the transverse momentum dependence (TMD) of the PDFs. Without integrating over the transverse dependence of the PDFs, gauge links couple soft and collinear portions of diagrams to the hard sub-graphs, breaking the factorization. Attempts to construct TMD factorization schemes, such as k_t -factorization [57, 58], have proven difficult and it has been shown explicitly that k_t -factorization is violated in high- p_T hadron production in hadronic collisions [59]. Building a framework to perform these types of calculations is still a subject under active development [60].

2.3.2 Deep Inelastic Scattering

The parton model was first developed in DIS, and this collision system will be used here to illustrate the utility of the factorized approach. In these collisions an electron interacts with a hadronic target of mass M via the exchange of a photon with large virtuality $q^2 = -Q^2$. In addition to Q^2 , the system is typically described in terms of the variables x and y

$$x = \frac{Q^2}{2q \cdot P}, \quad y = \frac{E - E'}{E}, \quad (2.19)$$

where P is the four-momentum of the target and E and E' are the initial and final energies of the electron as measured in the rest frame of the target. In the parton model, x corresponds to the fraction of target's momentum carried by the struck quark. The differential cross section is usually expressed in terms of structure functions F ,

$$\frac{d\sigma}{dx dy} = \frac{4\pi\alpha_{\text{EM}}^2}{xyQ^2} \left\{ y^2 x F_1(x, Q^2) + \left(1 - y - \frac{2Mxy}{2E} \right) F_2(x, Q^2) \right\}. \quad (2.20)$$

The observation of Bjorken scaling [9, 10], that for large Q^2 , F_1 and F_2 are independent of Q^2 , was the inspiration for the parton model. For spin- $\frac{1}{2}$ (charged)

partons, the structure functions obey the Callan-Gross relation $2xF_1 = F_2$. The experimental confirmation of this result provided support for the interpretation of spin- $\frac{1}{2}$ quarks. In collinear factorized form the structure functions have the form,

$$F_1(x, Q^2) = \sum_a \int_x^1 \frac{d\xi}{\xi} f_{a/A}(\xi, \mu^2, \mu_f) C_{1a} \left(\frac{x}{\xi}, \frac{Q^2}{\mu^2}, \frac{\mu_f^2}{\mu^2}, \alpha(\mu) \right) + \mathcal{O}(Q^{-2}), \quad (2.21a)$$

$$F_2(x, Q^2) = \sum_a \int_x^1 d\xi f_{a/A}(\xi, \mu^2, \mu_f) C_{2a} \left(\frac{x}{\xi}, \frac{Q^2}{\mu^2}, \frac{\mu_f^2}{\mu^2}, \alpha(\mu) \right) + \mathcal{O}(Q^{-2}). \quad (2.21b)$$

Here the functions $f_{a/A}$ are the PDFs for parton a in hadron A . The coefficient functions, C_a , are calculable in perturbation theory and are IRC safe. They are dominated by contributions of order Q ; propagators off shell by μ_f^2 will contribute to C_a while contributions below this scale are grouped into $f_{a/A}$. The result depends on both the factorization and renormalization scales, which need not be set equal.

Shortly after the computation of the β -function, similar renormalization group techniques were applied to the DIS structure functions, by considering moments of the PDFs (specifically non-singlet PDF, $f_q - f_{\bar{q}}$),

$$f^{(n)}(\mu^2) = \int_0^1 z^{n-1} f(z, \mu^2) dz. \quad (2.22)$$

These are related to the anomalous dimensions,

$$\gamma_n = \frac{d}{d \ln \mu} f^{(n)}(\mu^2), \quad (2.23)$$

which appear to give dimensions to dimensionless, but scale-dependent quantities through renormalization (e.g. $\ln f^{(n)} \sim \mu^{-\gamma_n}$), and can be computed in perturbation theory [19]. The Q -dependence of the PDF moments can be used to determine the Q -dependence of the moments of the structure functions,

$$\int x^{n-1} F_1(x, Q^2) dx = C_1^{(n)}(\alpha(Q^2)) f^{(n)}(Q_0^2) \times \exp \left[-\frac{1}{2} \int_0^{\ln Q^2/Q_0^2} dt \gamma_n(\alpha(Q_0^2 e^t)) \right]. \quad (2.24)$$

This relation predicts power-law scaling, $F_1(x, Q^2) \sim (Q/Q_0)^{-\alpha_0 \gamma_n / \pi}$, for theories that do not possess asymptotic freedom and posed a problem reconciling potential

theories with the observed scaling prior to the demonstration of asymptotic freedom in QCD. To one-loop in QCD the scaling is [23–26]

$$F_1(x, Q^2) \propto \left[\frac{\ln Q^2/\Lambda^2}{\ln Q_0^2/\Lambda^2} \right]^{-2\gamma_n/4|\beta_1|}. \quad (2.25)$$

This weak Q -dependence correctly described the early measurements of scaling in DIS, further building support for QCD as the correct theory of the strong interaction.

2.3.3 DGLAP and Parton Evolution

When calculating C_a , logarithms can arise due to the collinear emission at some scale Λ , which gives a factor of approximately

$$\alpha(Q^2) \ln \frac{Q^2}{\Lambda^2}. \quad (2.26)$$

These logarithms can become large such that the above product becomes of order unity. The result is that C_a will have large contributions from all orders and is shown schematically in Fig. 2.9. This multiple emission is enhanced by $\alpha(Q^2)^N \ln^N \frac{Q^2}{\Lambda^2}$, but only for the case where the virtualities are strongly ordered, $q_n^2 < q_{n-1}^2 < \dots < q_0^2$, with other orderings appearing with fewer powers of $\ln \frac{Q^2}{\Lambda^2}$.

The large logarithms are a symptom of interactions far away from the scale at which the coupling was fixed. Fortunately, these collinear contributions can be resummed by renormalization group methods. As most of the collinear emissions are well separated in scale from the probe, q_0 , these emissions can be reinterpreted as modifying the hadron structure as opposed to corrections to C_a . This results in a Q -dependence of the PDF that evolves the probe from the hard scale to lower momentum scales (indicated by the red sub-diagram in Fig. 2.9). For the change $Q \rightarrow Q + \Delta Q$ the differential probability of an emission with energy fraction z and transverse momentum $Q < p_\perp < Q + \Delta Q$ is given by

$$\frac{\alpha}{2\pi} \frac{dp_\perp^2}{p_\perp^2} P_{a \leftarrow b}(z) \simeq \frac{\alpha}{\pi} \frac{\Delta Q}{Q} P_{a \leftarrow b}(z), \quad (2.27)$$

where $P_{a \leftarrow b}(z)$ is the splitting function for parton of b splitting into type a , and can be computed from the diagrams shown in Fig. 2.10. Changes in the distribution of parton a at momentum fraction x can come from splittings of other partons at $x' = x/z$, and can be written as

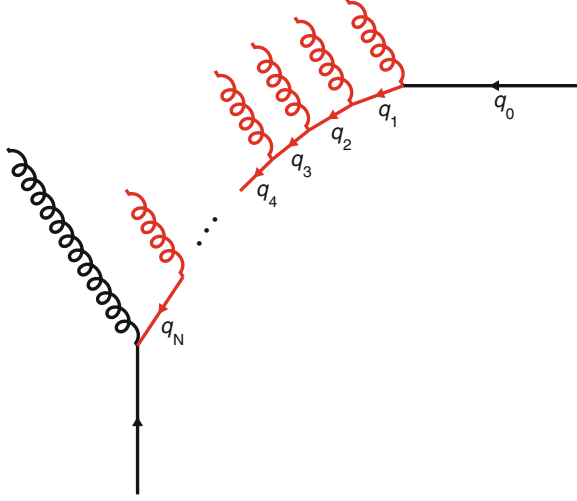


Fig. 2.9 Schematic representation of multiple collinear splittings. The portion of the diagram shown in *red* is interpreted as part of the structure of the struck hadron instead of a correction to the hard matrix element

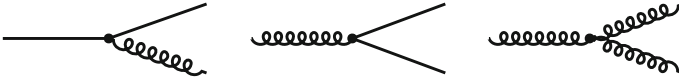


Fig. 2.10 Collinear QCD processes used to compute splitting functions

$$\begin{aligned}
 \Delta f_a(x, Q) &= \sum_b \int_0^1 dx' \int_0^1 dz \frac{\alpha}{\pi} \frac{\Delta Q}{Q} P_{a \leftarrow b}(z) f_b(x', Q) \delta(x - zx') \\
 &= \Delta \ln Q \sum_b \frac{\alpha}{\pi} \int_x^1 \frac{dz}{z} f_b\left(\frac{x}{z}, Q^2\right) P_{a \leftarrow b}(z).
 \end{aligned} \tag{2.28}$$

These lead to the DGLAP evolution equations [61–63] which are of the form

$$\frac{\partial}{\partial \ln Q} f_a(x, Q) = \sum_b \frac{\alpha}{\pi} \int_x^1 \frac{dz}{z} f_b\left(\frac{x}{z}, Q^2\right) P_{a \leftarrow b}(z). \tag{2.29}$$

See Ref. [29] for a complete tabulation of the splitting functions and full evolution equations. This result indicates that if f_a is measured as a function of x at a given value of Q_0 , the PDF at any other scale Q can be determined by evolving the PDF according to Eq. 2.29. The Q^2 dependence of the structure function F_2 at fixed x is

shown in Fig. 2.1. This dependence agrees well with the dependence predicted by the DGLAP equations over a range of Q^2 and x values.

2.3.4 Fragmentation Functions

The final-state analog of the parton distribution function is known as a fragmentation function. The fragmentation function $D_i^h(z, \mu^2)$ encapsulates the probability that a parton of type i will fragment into a hadron of type h with momentum fraction z of the original parton. In e^+e^- collisions, where there are no initial parton distributions, cross sections for the production of a particular species of hadron can be written as,

$$\frac{d\sigma_{e^+e^-}^h}{dx} = \sum_i \int_x^1 \frac{dz}{z} C_i \left(z, \alpha_S(\mu^2), \frac{s}{\mu^2} \right) D_i^h(z, \mu^2) + \mathcal{O} \left(\frac{1}{\sqrt{s}} \right). \quad (2.30)$$

For situations with arbitrary numbers initial/final-state hadrons, the collinear factorized relation takes the form of Eq. 2.18. The e^+e^- measurements provide the cleanest access to the fragmentation functions since there is no integration over PDFs. The fragmentation functions obey an evolution equation in μ^2 identical to Eq. 2.29, with the inverse splitting functions (i.e. $P_{a \leftarrow b}(z)$ is replaced with $P_{a \rightarrow b}(z)$). In the parton model these obey the momentum sum rule,

$$\sum_h \int_0^1 dz z D_i^h(z, \mu^2) = 1. \quad (2.31)$$

The higher-order corrections to the splitting functions can see logarithmic enhancements at low x , an effect which causes the leading order approximation of the evolution to break down much sooner in e^+e^- than DIS. This has led to development of calculations using a modified leading log approximation (MLLA), which include corrections for next-to-leading effects [64–68]. In general, the behavior of these enhancements is to cause the “hump-backed plateau” behavior,

$$x D(x, s) \propto \exp \left\{ -\frac{1}{2\sigma^2} (\xi - \xi_p)^2 \right\}, \quad (2.32)$$

with $\xi = \ln 1/x$ and the width and peak approximately given by [69],

$$\xi_p \simeq \frac{1}{4} \ln s / \Lambda^2, \quad \sigma \propto \left(\ln s / \Lambda^2 \right)^{3/4}. \quad (2.33)$$

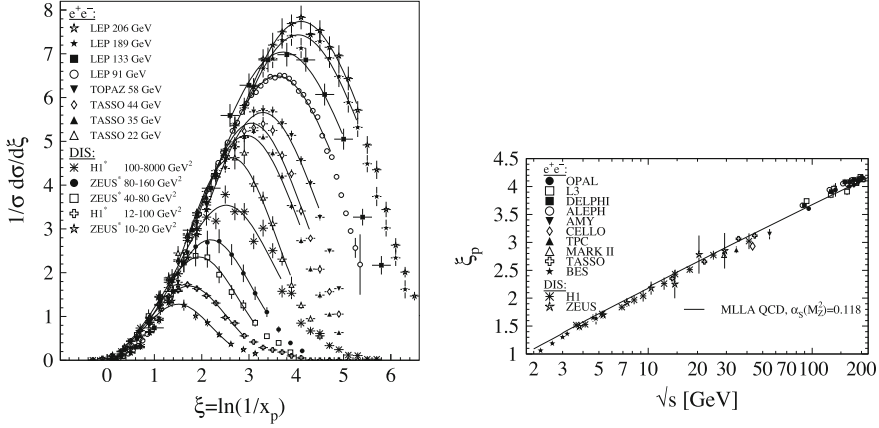


Fig. 2.11 The hump-backed plateau structure of fragmentation functions through the measurement of single inclusive hadron cross sections (*left*). The cross sections are fit with a Gaussian and the extracted peak position compares well with the MLLA QCD prediction (*right*). Figure adapted from Ref. [29]

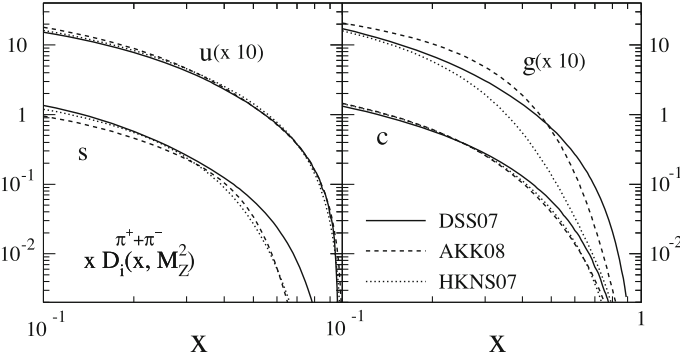


Fig. 2.12 Contributions to the $\pi^+\pi^-$ NLO fragmentation functions from up, strange (*left*), gluon and charm (*right*) from three different global analyses [70–72], with $Q^2 = m_Z^2$. Figure adapted from Ref. [29]

This behavior is shown in Fig. 2.11, with the fragmentation functions fit with a Gaussian for a variety of \sqrt{s} and Q^2 values shown on the right and a comparison of the extracted peak position to the MLLA value shown on the left.

To span a large kinematic range and provide separation between quark and anti-quark contributions, the e^+e^- data has been supplemented by DIS and hadronic collider data in recent global NLO extractions [70–72] (see Sect. 2.3.5 for discussion of fixed order calculations). A comparison of results of some such analyses are shown in Fig. 2.12, where the various partonic contributions to the charged pion fragmentation function are shown.

2.3.5 Fixed Order Calculations

Perturbative calculations are typically performed at fixed order and it is useful to consider IRC safety in this context [29]. For an n -particle process, the cross section for an observable, \mathcal{O}_n , can be constructed at leading order (LO) as

$$\sigma_{\mathcal{O}, \text{LO}} = \alpha_S^{n-2}(\mu_R) \int d\Omega_n |M_{n,0}^2|(p_1, \dots, p_n) \mathcal{O}_n(p_1, \dots, p_n), \quad (2.34)$$

where $M_{n,0}^2$ is the n -particle matrix element at tree-level, $d\Omega_n$ is the measure over the n -particle phase space and μ_R is the renormalization scale. Non-perturbative corrections have been omitted here. The tree-level amplitudes are finite but the integral will diverge in the soft and collinear regions of the momentum integration. Therefore this calculation is only safe when \mathcal{O}_n also vanishes in this limit (e.g. jet cross sections). At next-to-leading-order (NLO) the $n + 1$ -particle matrix element must be considered along with the interference between the tree-level and 1-loop n -particle processes,

$$\begin{aligned} \sigma_{\mathcal{O}, \text{NLO}} = & \sigma_{\mathcal{O}, \text{LO}} \\ & + \alpha_S^{n-1}(\mu_R) \int d\Omega_{n+1} |M_{n+1,0}^2|(p_1, \dots, p_{n+1}) \mathcal{O}_{n+1}(p_1, \dots, p_{n+1}) \\ & + \alpha_S^{n-1}(\mu_R) \int d\Omega_n 2\text{Re} [M_{n,0} M_{n,1}^*](p_1, \dots, p_n) \mathcal{O}_n(p_1, \dots, p_n). \end{aligned} \quad (2.35)$$

Here $M_{n,1}$ is the 1-loop n -particle amplitude, which diverges in the soft and collinear limits. This divergence will cancel with the aforementioned tree-level divergence in the integration if the observable is IRC safe,

$$\begin{aligned} \lim_{p_i \rightarrow 0} \mathcal{O}_{n+1}(p_1, \dots, p_i, \dots, p_{n+1}) &= \mathcal{O}_n(p_1, \dots, p_n) \\ \lim_{p_j \parallel p_i} \mathcal{O}_{n+1}(p_1, \dots, p_i, p_j, \dots, p_{n+1}) &= \mathcal{O}_n(p_1, \dots, p_i, \dots, p_n). \end{aligned} \quad (2.36)$$

A similar procedure applies in extending to NNLO calculations, which involve additional contributions the tree-level $n + 2$ contribution, interference between tree-level and 1-loop $n + 1$ -particle diagrams, interference between the n -particle tree-level and 2-loop diagrams and the squared contribution of the 1-loop n -particle diagram. These calculations become increasingly difficult to compute, especially in an automated fashion, due to the intricate higher-loop diagrams.

Often these calculations are supplied in the form of Monte Carlo event generators. These tools typically compute a hard scattering matrix element and then evolve the partons by means of a parton shower. This technique constructs a probability for a parton not split from the splitting functions defined in Eq. 2.27. The probability that a parton of type a will not split between scales Q^2 and Q_0^2 , $\Delta_a(Q^2, Q_0^2)$, known as a Sudakov form factor is given by,

$$\Delta_a(Q^2, Q_0^2) = \exp \left\{ - \int_{Q_0^2}^{Q^2} \frac{dk_t^2}{k_t^2} \int_0^1 dz \frac{\alpha_S}{2\pi} \sum_b P_{a \leftarrow b}(z) \right\}. \quad (2.37)$$

MC sampling determines the scale of the first splitting, and this process is repeated down to some hadronization scale $Q \sim 1$ GeV. At this point a hadronization model [48, 49, 73, 74] converts the evolved partons into final-state hadrons which can be used to simulate response of a detector to an input physics signal. Leading order event generators (e.g. PYTHIA) typically give the correct description of the soft and collinear emission, but fail to describe wide angle emissions due to the lack of multi-parton matrix elements. This can be improved by generators which use this higher order matrix elements and merge the parton showers in such a way as to avoid double counting the real and virtual contributions [75–78].

In general LO calculations for applications at hadron colliders are accurate to approximately a factor of two. A K -factor, which represents the ratio of NLO to LO contributions, is typically used to tune the cross sections.

2.3.6 Jets

Highly collimated sprays of particles known as jets are a ubiquitous feature of high energy particle collisions. These objects are the experimental signature of partonic hard scattering processes and have been used to test the theoretical application of the theory since their initial observation at SLAC [33]. However, the multi-particle final states associated with jet production are sufficiently complicated that any experimental measurement must have a precise definition of an observable [37]. Furthermore, these definitions must be relatable to quantities that are well-defined theoretically, particularly with regard to the IRC safety issues discussed previously.

Most early jet algorithms were based on associating particles or energy deposits that were nearby in angle, typically referred to as cone algorithms. The Snowmass workshop in 1990 [79] proposed a standard set of criteria for jet algorithms [80], however, implementations of these criteria were not immediately obvious. Many cone algorithms used at the time suffered from varying degrees of IRC unsafety, which limited their relatability to theory [81]. The effects of unsafety are illustrated in Fig. 2.13, where two algorithms, one safe (left) and one unsafe (right) are compared. In the IRC safe algorithm, the emission of a collinear gluon does not affect the clustering (b), allowing the divergence in this graph to cancel the 1-loop (a) divergence. However, this emission causes different clustering in the unsafe algorithm (d), resulting in a failure in cancellation of the divergences. In general, issues of split or overlapping jets are not handled in a natural way by cone algorithms, and some additional criteria, often introducing undesired artifacts, are required to handle such cases.

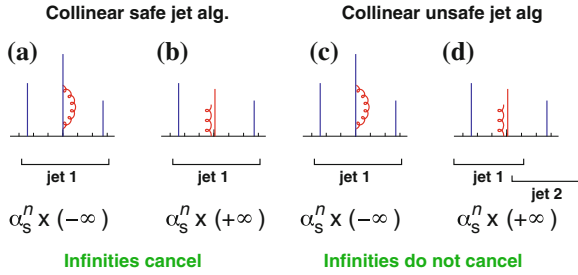


Fig. 2.13 Jet reconstruction using two algorithms on a system with and without additional collinear gluon radiation. The IRC safe algorithm reconstructs the two scenarios as the same jet (**a**, **b**), allowing for cancellation of divergences. The unsafe algorithm gives different results in the two cases (**c**, **d**). Figure adapted from Ref. [82]

Sequential clustering algorithms, which perform pairwise clustering of particles [83, 84], showed particular promise as they were IRC safe. This led to the proposal for the k_t algorithm in e^+e^- collisions [85], which was formulated to be boost-invariant and IRC safe and was later adapted for hadronic collisions [86]. The inclusive formulation of this algorithm [87] uses the measure,

$$d_{ij} = \min \left(p_{Ti}^2, p_{Tj}^2 \right) \frac{\Delta R_{ij}^2}{R^2}, \quad \Delta R_{ij}^2 = (y_i - y_j)^2 + (\phi_i - \phi_j)^2, \quad (2.38)$$

where y and ϕ are the particles' rapidity and azimuthal angle respectively, to cluster nearby particles. The algorithm works using the following steps:

1. Calculate d_{ij} for all pairs and also $d_{iB} = p_{Ti}^2$.
2. Find the minimum of the d_{ij} and d_{iB} .
3. If the minimum is a d_{ij} , combine i and j and start over.
4. If the minimum is a d_{iB} , call i a final-state jet and remove it from subsequent clustering and start over.
5. Finish clustering when no particles remain.

The parameter R controls the size of the jets in analogy with the radius parameter in cone jets. In this inclusive form, all particles are clustered into final-state jets; thus some final discriminating criteria, often a minimum cut on E_T or p_T , must be applied. This algorithm has the feature that for soft or collinear pairs the distance measure is inversely proportional to the differential probability of collinear emission,

$$\frac{dP_{k \rightarrow ij}}{dE_i d\theta_{ij}} \sim \frac{\alpha_s}{\min(E_j, E_j)\theta_{ij}}, \quad (2.39)$$

which is easily adaptable to theoretical calculations [81]. This algorithm was not originally favored by experiment due to its slow processing time and geometrically irregular jets, which made experimental corrections more difficult. However, a faster

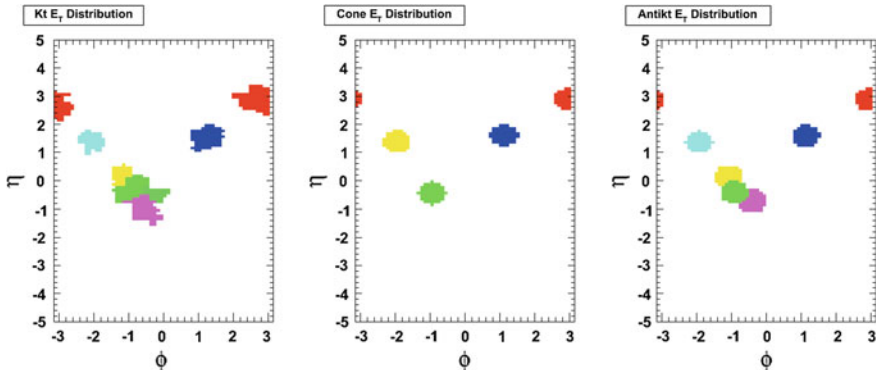


Fig. 2.14 Jet clustering on an event in $\eta - \phi$ using three different jet algorithms: k_t (left), ATLAS cone (center), and anti- k_t (right) all with $R = 0.4$. The cone algorithm does a poor job of resolving the split jet. The k_t and anti- k_t resolve this as two separate jets, but the k_t clustering is strongly influenced by other soft particles in the event

implementation by the `FastJet` package ($\mathcal{O}(N \ln N)$ vs. $\mathcal{O}(N^3)$) has significantly improved the former issue [88].

The distance measure of the k_t algorithm can be generalized in the following way:

$$d_{ij} = \min \left(p_{Ti}^{2p} p_{Tj}^{2p} \right) \frac{\Delta R_{ij}^2}{R^2}. \quad (2.40)$$

The choice $p = 1$ corresponds to the usual k_t algorithm, while $p = 0$ corresponds to the Cambridge/Aachen algorithm [89, 90], which uses only geometric considerations when clustering objects. The generalization was used to define the anti- k_t algorithm ($p = -1$), which clusters hard particles first and produces jets similar with regular, cone-like geometry [82]. Examples of the clustering behavior of the k_t , ATLAS cone [91] and anti- k_t algorithms are shown Fig. 2.14. The k_t allows jets clustered from soft background particles to compete with the real jet signal, a feature which is particularly problematic in heavy ion collisions. This is contrasted by the behavior of the anti- k_t which preferentially clusters particles with the harder of two jets.

Jets have become an essential part of high energy experiments, both as tools for testing QCD, but also as input into reconstructing more complicated physics objects. Figure 2.15 shows the data/theory ratio for the inclusive jet cross section as a function of jet p_T for a wide range of experiments. The theoretical calculation is provided by `fastNLO` with `NLOJET++` [92].

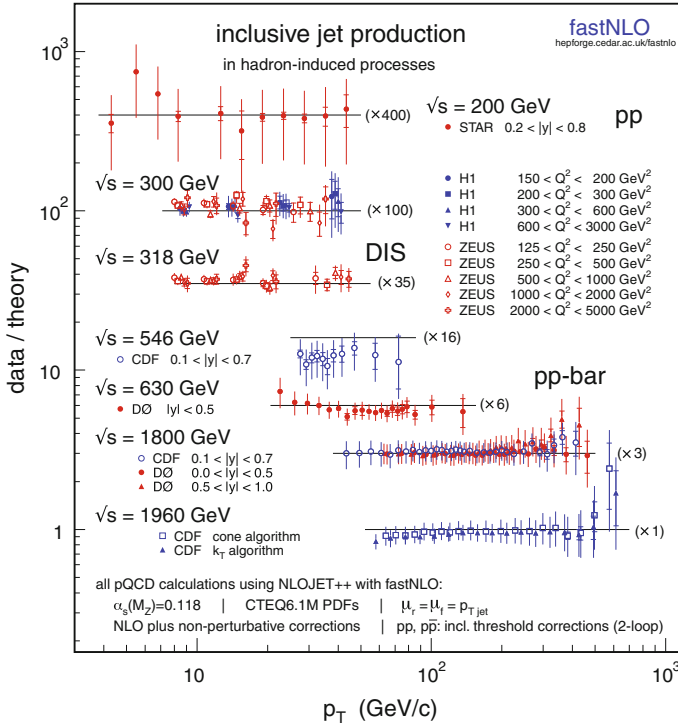


Fig. 2.15 Ratio of data to theory for the single inclusive jet cross section at a variety of energies [29, 92]

2.4 Phase Structure of Nuclear Matter

Prior to the advent of QCD, attempts were made to apply statistical methods to the large particle multiplicities in high energy collisions [93, 94]. This led to the analysis of the high temperature limit of nuclear matter in the context of hadronic resonances. The growth in the number of these resonance states with increasing energy led Hagedorn to propose the Statistical Bootstrap Model, where resonances are thought of as being composed of excited lower mass resonance constituents. In the high temperature limit the density of resonant states and the thermodynamic energy density of states approach each other and the partition function diverges. The temperature cannot be increased beyond some limiting value, the Hagedorn temperature, as adding energy will only excite more resonances, not add to the kinetic energy of the system [95].

Asymptotic freedom indicates that this will not occur, but rather that at sufficiently high temperatures the coupling will become weak leading to nuclear matter with dynamics described by perturbative QCD [96]. This suggests that there is a phase transition where the degrees of freedom evolve from hadrons to quarks and gluons.

This state of matter the Quark Gluon Plasma (QGP), represents the form of nuclear matter in the early stages of the Universe [97].

In the weak coupling limit the Stefan-Boltzmann relation between energy density, ε , and pressure, p , applies:

$$\varepsilon - 3p = 0. \quad (2.41)$$

Each is proportional to T^4 with the constant of proportionality indicating the degeneracy of particles obeying Bose-Einstein, g_{BE} , and Fermi-Dirac, g_{FD} , statistics,

$$\varepsilon = \left(g_{\text{BE}} + \frac{7}{8} g_{\text{FD}} \right) \frac{\pi^2}{30} T^4. \quad (2.42)$$

At the lowest temperatures the system is hadron gas containing only the lowest state, the pions ($g_{\text{BE}} = 3_{\text{isospin}}$, $g_{\text{FD}} = 0$). At high temperature the system is a gas of deconfined quarks and gluons ($g_{\text{BE}} = 8_{\text{color}} \times 2_{\text{spin}}$, $g_{\text{FD}} = 3_{\text{color}} \times 2_{\text{spin}} \times 2_{q\bar{q}} \times N_f$). The total energy density is

$$\varepsilon = \frac{\pi^2}{30} T^4 \begin{cases} 3 & T \sim 0 \\ 16 + \frac{21}{2} N_f & T \rightarrow \infty \end{cases}. \quad (2.43)$$

For two flavor QCD the difference in phases corresponds to a factor of 9 increase in ε/T^4 , indicating a dramatic change in energy density.

The temperature range over which this transition occurs, specifically the possible divergences of thermodynamic variables, can characterize the transition. In the limit of zero quark mass, the QCD Lagrangian possesses chiral symmetry, which is broken by non-perturbative effects resulting in three massless pions. The high temperature limit exhibits both deconfinement and restoration of chiral symmetry, and it is unclear to what extent these two phenomena are interrelated and whether QCD may exhibit a distinct phase transition associated with each of these phenomena [98].

2.4.1 Thermal Field Theory

The extension to finite-temperature field theory is accomplished by using the relationship between the path integral formulation in quantum field theory and the partition function of statistical mechanics [99, 100]. Explicitly, the path integral for a single quantum mechanical particle with Hamiltonian H is given by

$$\langle q'(t) | e^{-i\hat{H}t} | q(0) \rangle = \int_{q(0)}^{q'(t)} \mathcal{D}[q(t)] e^{i \int_0^t dt' L}, \quad (2.44)$$

which denotes the amplitude for a particle at q at $t = 0$ to go to q' at t , and $L = \frac{1}{2}m\dot{q}(t)^2 - V(q(t))$. This functional integral can be analytically continued to imaginary time via $t \rightarrow -i\tau$. This generally provides a more rigorous definition for the path integral and its convergence. In the imaginary time formulation the action in the exponent is replaced by the Euclidean action

$$S_E = \int_0^\tau d\tau' L_E(\tau'), \quad (2.45)$$

where $L_E = \frac{1}{2}m\dot{q}(t)^2 + V(q(t))$. This can be compared directly to the partition function of the canonical ensemble, with temperature T and $\beta = 1/kT$, $Z(\beta) = \text{Tr}[e^{-\beta\hat{H}}]$. In the non-diagonal basis $|q\rangle$ this can be written in the same form as the usual path integral,

$$Z(\beta) = \int dq \langle q | e^{-\beta\hat{H}} | q \rangle = \int_{q(0)=q(\tau)} \mathcal{D}[q(\tau)] e^{-\int_0^\beta d\tau' L_E} \quad (2.46)$$

Thermal expectation values of time-ordered products of fields $\langle \cdots \rangle_\beta$ can be computed in the same fashion as zero-temperature field theory, but using the imaginary time/Euclidean action. For example, a generating functional, $Z(\beta, \mathcal{J})$, can be constructed by introducing a source \mathcal{J} , and adding the term $\mathcal{J}\hat{q}$ to the Lagrangian. A two-point correlation function can be evaluated with functional derivatives with respect to \mathcal{J} ,

$$\Delta(\tau) = \langle T \hat{q}(-i\tau) \hat{q}(0) \rangle_\beta = \frac{1}{Z(\beta, 0)} \frac{\delta^2 Z(\beta, \mathcal{J})}{\delta \mathcal{J}(\tau) \delta \mathcal{J}(0)} \Big|_{\mathcal{J}=0}. \quad (2.47)$$

The cyclic nature of the trace imposes the constraint $\Delta(\tau - \beta) = \pm \Delta(\tau)$, with the sign depending on whether the field obeys commutation or anti-commutation relations. Thus the periodic (anti-periodic) boundary conditions on the correlation functions enforce the Bose-Einstein (Fermi-Dirac) statistics and Δ can be described as a Fourier series

$$\Delta(\tau) = \beta \sum_{n=0}^{\infty} e^{-i\omega_n \tau} \Delta(i\omega_n). \quad (2.48)$$

Here $\omega_n = \frac{2\pi n}{\beta}$ for bosons and $\omega_n = \frac{\pi(2n+1)}{\beta}$ for fermions and are known as the Matsubara frequencies. The full real-time gauge theory propagators at tree level are

$$D_F(k_0) = \frac{i}{k_0^2 - \omega^2 + i\epsilon} + 2\pi\delta(k_0^2 - \omega^2) \frac{1}{e^{\beta k_0} - 1}, \quad (2.49a)$$

$$S(p) = \frac{i}{\not{p} - m} + 2\pi\delta(p^2 - m^2)(\not{p} + m)\frac{1}{e^{\beta p_0} + 1}, \quad (2.49b)$$

for the bosons and fermions respectively. In both expressions, the first term describes the usual vacuum propagation while the second represents the disconnected part of the propagation which counts the modes absorbed by the medium.

2.4.2 Lattice Thermodynamics

The lattice formulation of QCD discussed previously can be naturally applied to calculate thermodynamic variables in QCD, since it is formulated as a Euclidean space-time evaluated path integral. The four-dimensional Euclidean space-time is represented by $N_\sigma^3 \times N_\tau$ lattice sites with spacing a . The system is described by volume V and temperature, T ,

$$V = (N_\sigma a)^3, \quad T = \frac{1}{N_\tau a}, \quad (2.50)$$

and the thermodynamic limit is taken with $N_\tau \rightarrow \infty$, $a \rightarrow 0$ but holding T fixed. Statistical errors can enter since the integration is performed over a finite number of gauge field configurations, thus making calculations with large N_τ difficult. Recent developments in improved actions with reduced discretization errors allow for accurate calculations without resorting to large N_τ , and have facilitated advances in lattice thermodynamic calculations.

Typically the action is separated into a contribution from the gauge fields and a fermionic contribution. The latter is expressed as a functional determinant in a way that removes or minimizes fermion doubling problems. The action and determinant are written in terms of link variables, which involve the evaluation of gauge field configurations at adjacent lattice sites. The numerical integration techniques require a probabilistic interpretation, and problems occur when the determinant becomes negative. For zero chemical potential, μ , this is not a problem, however, the determinant becomes complex-valued for $\mu \neq 0$. This makes calculations at finite chemical potential more difficult, although recent advances have been made on this subject.

The QCD equation of state can be determined on the lattice by evaluating the trace anomaly (the trace of the stress-energy tensor $\Theta^{\mu\nu}(T)$) in the grand canonical ensemble,

$$\frac{\Theta^{\mu\mu}}{T^4} = \frac{\varepsilon - 3p}{T^4} = T \frac{\partial}{\partial T} \left(\frac{p}{T^4} \right). \quad (2.51)$$

Since only expectation values can be calculated, the variables must be re-expressed in this form. The pressure can be evaluated directly from integrating the trace anomaly. The entropy density, s , and speed of sound c_s , can likewise be calculated from the relations

$$\frac{s}{T^3} = \frac{\varepsilon + p}{T^4}, \quad c_s^2 = \frac{dp}{d\varepsilon}. \quad (2.52)$$

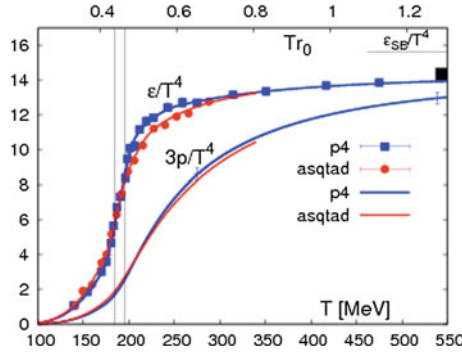


Fig. 2.16 Pressure and energy density divided by T^4 as a function of temperature in a lattice calculation using physical quark masses [101]

The pressure and energy density divided by T^4 from a recent calculation [101] are shown in Fig. 2.16. The lattice results indicate a rapid, but continuous transition in ε at $T_C \sim 170$ MeV, which is not indicative of a first or second order phase transition, but rather a smooth crossover between phases. Additionally, order parameters describing the transition to deconfinement and the restoration of chiral symmetry have been formulated on the lattice. The deconfinement order parameter is the expectation value of the Polyakov loop, $\langle L \rangle \sim \exp(-F_q(T)/T)$ where F_q is the static free quark energy. The chiral transition is described by the chiral susceptibility $\chi = -\frac{\partial}{\partial m} \langle q\bar{q} \rangle \Big|_{m=0}$. These quantities involve subtleties relating to their renormalization and corrections due to finite quark masses. A calculation of these two quantities [101] is shown in Fig. 2.17. The results indicate that both of these transitions occur smoothly over the same temperature region where the equation of state shows a rapid change in energy density.

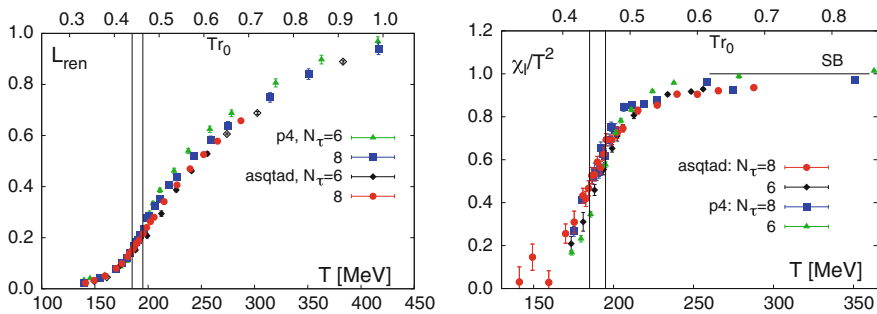


Fig. 2.17 Lattice calculations of the $\langle L \rangle$ (left) and χ/T^2 (right) for light quarks as functions of temperature. These are order parameters for the deconfinement and chiral symmetry restoration transitions respectively. The vertical lines indicate the temperature range over which the rapid cross over is inferred to occur from the equation of state. Figure adapted from Ref. [101]

2.4.3 The Hard Thermal Loop Approximation

When using perturbation theory at finite temperature, including the effects of loops becomes problematic as the finite scale introduced by T breaks the usual perturbative expansion. If the external momenta are hard, all loops will contribute to the same order as the tree level diagram. However, if the external momenta are soft, $P \sim gT$, only the contribution from Hard Thermal Loops (HTLs) will compete with the tree level term. These are cases where the “hard” loop momenta are much greater than the “soft” external momenta and the dominant contribution to the loop comes from momenta of order T . In gauge theories, the HTLs can be identified by power counting and an effective theory of resummed HTLs can be derived without affecting the vacuum renormalizability properties of the theory [102, 103]. These loops lead to the generation of thermal masses m and m_f for the gauge bosons and fermions respectively. The static component of the gauge boson propagator takes the form

$$D_{00} = \frac{-i}{\vec{q}^2 + 2m^2}, \quad (2.53)$$

where the thermal mass gives rise to Debye screening. In the static limit, $\omega/q \rightarrow 0$, the magnetic behavior is similar to the above expression, but with

$$m^2 \rightarrow \frac{\pi m^2}{2} \frac{\omega}{q}. \quad (2.54)$$

This can be interpreted as a frequency-dependent dynamical screening with cutoff $m\sqrt{\frac{\pi\omega}{2q}}$, which is in some cases effective in protecting infrared divergences [104]. The full thermal masses including the effects from a finite chemical potential, μ , are given by

$$m^2 = \frac{1}{6}g^2T^2C_A + \frac{1}{12}g^2C_F\left(T^2 + \frac{3}{\pi^2}\mu^2\right), \quad (2.55a)$$

$$m_f^2 = \frac{1}{8}g^2\left(T^2 + \frac{1}{\pi^2}\mu^2\right)C_F, \quad (2.55b)$$

with the color factors given previously in Eq. 2.8.

One issue that is still not fully understood is the screening of the chromomagnetic fields. Using power counting arguments it can be shown that a diagram containing $\ell + 1$ gluon loops, shown in Fig. 2.18, with $\ell > 3$, has infrared divergences of the form [105]

$$g^6T^4\left(\frac{g^2T}{m}\right)^{\ell-3}. \quad (2.56)$$

For the longitudinal components this is regulated by the electric mass and gives behavior $\sim g^{\ell+3}T^4$, which differs from the $g^{2\ell}$ behavior expected from perturbation

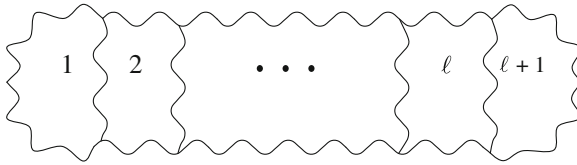


Fig. 2.18 Diagram containing $\ell + 1$ gluon loops

theory. Based on arguments from theories that are infrared-equivalent to QCD, the magnetic mass is of order $\sim g^2 T$ [106]. This leads to infrared divergences in the transverse part of the $\ell + 1$ gluon loop diagram to go as $\sim g^6 T^4$ and signals a total breakdown of perturbation theory. This remains an outstanding problem, with thermal field theory not on rigorous theoretical ground except at asymptotically high temperatures.

2.4.4 Heavy Ion Collisions

The phase structure predicted by the lattice indicates that at low baryon chemical potential and high temperature, hadronic matter undergoes a rapid, but continuous increase in the number of degrees of freedom. This transition is illustrated in a possible QCD phase diagram, shown in Fig. 2.19. In addition to this transition, abnormal forms of nuclear matter can exist at high densities [107, 108]. Astrophysical objects such as neutron stars are stabilized against gravitational collapse by the degeneracy pressure created by an extremely high density of neutrons. At the highest densities novel states such as quark liquids and color superconductors (color flavor locked) are thought to exist [109].

It is believed that the QGP transition is experimentally accessible in collisions among heavy ions at high energies. In these collisions the nuclei appear as highly Lorentz contracted “pancakes” [110]. Particle production occurs as the two pancakes overlap leaving a “central” region of high energy density as they recede and carry away the net baryon density (leading baryon effect). If the system is formed after some time t_f , the energy density in this region can be estimated following the Bjorken procedure by considering the total energy per unit rapidity in nucleus-nucleus collisions, $\frac{dE_T}{dy}$. The energy density is then

$$\varepsilon = \frac{dE_T}{dy} \Delta y \frac{1}{V}. \quad (2.57)$$

For a small slice along the beam direction $\Delta y = \frac{\Delta z}{t_f}$, and $V = \pi R_A^2 \Delta z$. R_A is the nuclear radius and behaves as $R_A \simeq 1.2 A^{1/3}$ fm. The energy density can be expressed as

$$\varepsilon = \frac{1}{\pi R_A^2 t_f} \frac{dE_T}{dy}. \quad (2.58)$$

For Au¹⁹⁷ collisions at RHIC, $\frac{dE_T}{dy}$ was measured by PHENIX to be 688 GeV at $\sqrt{s_{NN}} = 130$ GeV [111]. If the formation time is on the order of 0.1–1 fm, this procedure gives an energy density estimate of 4.6–46 GeV/fm³. The Stefan-Boltzmann equation of state can be used to infer a temperature,

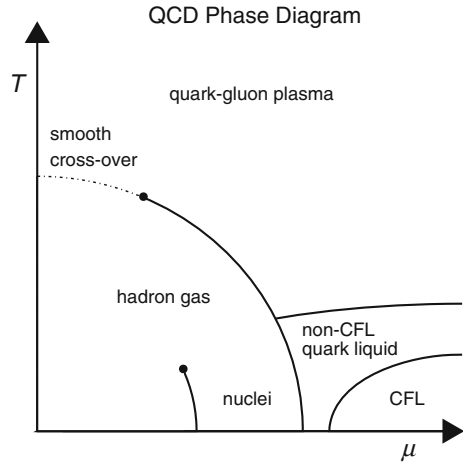
$$T \simeq \left(\frac{\varepsilon (\hbar c)^3}{\alpha} \right)^{1/4}, \quad (2.59)$$

where $\alpha = \frac{30}{\pi^2} (16 + \frac{21}{2} N_f)$ is a constant of proportionality determined by the effective number of degrees of freedom. Since the lattice results indicate that this limit is not reached a more appropriate estimate would be to use the lattice value of $\alpha = \varepsilon/T^4 \simeq 13$, just above the transition region. This estimate gives a temperature of $128 \lesssim T \lesssim 229$ MeV. The transverse energy density in Pb+Pb collisions at the LHC at $\sqrt{s_{NN}} = 2.76$ TeV is larger than at RHIC by roughly a factor of 5, indicating a temperature range of $191 \lesssim T \lesssim 342$ MeV. As the temperature region of the phase transition is spanned by these estimates, it is likely that such a transition is probed in relativistic heavy ion collisions.

If the mean free path in the interacting system is small compared to the system size a hydrodynamic description can be applied to the created nuclear matter [94]. The evolution of the system in the absence of viscosity or heat conduction is described by ideal hydrodynamics,

$$\partial_\mu T^{\mu\nu} = 0, \quad T^{\mu\nu} = (\varepsilon + p)u^\mu u^\nu - pg^{\mu\nu}, \quad (2.60)$$

Fig. 2.19 The QCD phase diagram. The transition is believed to possess a critical point where the first-order phase transition between hadron gas to PCP changes to a smooth cross over



where $T^{\mu\nu}$ is the relativistic stress-energy tensor, u^μ is the local four-velocity of a fluid element and the system of equations is closed by a thermodynamic equation of state. The Bjorken picture considers the longitudinal expansion of this medium which leads to a slow decrease in the temperature, $T \sim \tau^{-1/3}$, where τ is the local fluid proper time, and constant entropy inside the co-moving fluid volumes.

Local anisotropies in the transverse density of produced particles can be produced through initial-state fluctuations or more commonly through the elliptical geometry of the collision zone when there is incomplete nuclear overlap. As the particle production is isotropic, the only way this can be converted to a momentum-space anisotropy, is if these density fluctuations form pressure gradients, which result in radial flow. Such an effect should be observable in the angular distribution of hadrons and may allow for a determination of the fluid's shear viscosity, η .

Calculational techniques in string theory have established a correspondence between quantum field theories and their dual gravity theories. This AdS/CFT correspondence facilitates a translation between quantities in a gravity calculation in the weakly coupled region to quantities in the strongly coupled regime of the appropriate dual [112, 113]. In particular the thermodynamics of black hole can be mapped to thermodynamics in QCD-like $\mathcal{N} = 4$ supersymmetric Yang-Mills theory. Some time ago, arguments based on the uncertainty principle suggested that there is a quantum lower limit to the viscosity [114]. This has been demonstrated explicitly in the AdS/CFT picture where a limiting value of the viscosity to entropy density ratio was found to be $\eta/s \leq 1/4\pi$ [115, 116].

This application of hydrodynamics illustrates how the transport properties of the system can provide further insight into the dynamics of the medium, in particular through transport coefficients such as the shear viscosity, which are sensitive to the microscopic behavior. As a transport phenomenon, hydrodynamics coincides with the long-wavelength behavior of the system and the relevant transport and other phenomena such as radiation and diffusion can provide access to other aspects of the medium.

2.5 Hard Processes in Nuclear Collisions

2.5.1 The Glauber Model

In collider experiments, the measured rates of quantities are proportional to the luminosity, or instantaneous flux of colliding particles. At high energies, the nuclear size is easily resolved, and a beam constituent not only sees a flux of nuclei but an instantaneous flux of nucleons/partons determined by the geometric overlap between the colliding nuclei. For two nuclei, A and B, with centers separated by impact parameter \mathbf{b} , this flux is represented by the factor $T_{AB}(\mathbf{b})$. Many nuclear effects are expected to vary with \mathbf{b} , and T_{AB} is often used to normalize quantities to remove any variation due to trivial geometric effects. Experimentally, events are grouped into different centrality classes, which are determined to have a similar amount of

geometric overlap based on a set of global event criteria. The average T_{AB} is used to normalize quantities observed in those events to assess the centrality dependence of an observable. This procedure makes use of a framework known as the Glauber Model [117–119] and is employed by nearly all heavy ion experiments [120].

The Glauber Model treats the incoming nuclei as smooth distributions of nucleons, each traveling on independent linear trajectories. It is formulated in the optical limit, in which the overall phase shift is evaluated by summing over all per-nucleon pair phase shifts. It relies on a parametrization of the nuclear density, ρ , typically a two-parameter Woods-Saxon distribution,

$$\rho(r) = \rho_0 \frac{1}{1 + \exp\left(\frac{r-R}{a}\right)}, \quad (2.61)$$

where R and a are experimentally determined parameters, describing the radius and skin depth of the nucleus. The constant ρ_0 is an overall normalization factor ensuring the distribution is normalized to the number of nucleons. For Pb^{208} these parameters are $R = 6.62 \pm 0.06$ fm, $a = 0.546 \pm 0.01$ fm [121] and the distribution is shown in Fig. 2.20.

In the Glauber formalism the transverse density,

$$T_A(\mathbf{b}') = \int dz_A \rho_A(\mathbf{b}', z_A) \quad (2.62)$$

is the expected number of nucleons at position \mathbf{b}' . Then T_{AB} is defined as AB times the probability to simultaneously find nucleons in nuclei A and B at the same position \mathbf{b} as shown in Fig. 2.21,

$$T_{AB}(\mathbf{b}) = \int d^2b' T_A(\mathbf{b}') T_B(\mathbf{b}' - \mathbf{b}). \quad (2.63)$$

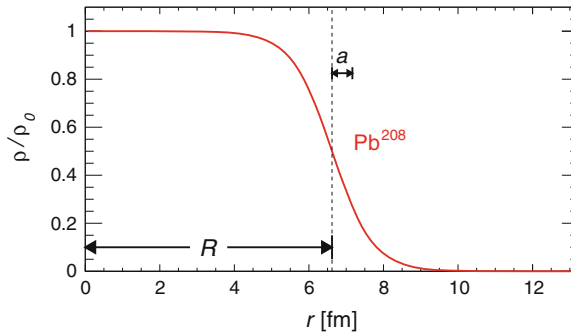


Fig. 2.20 Woods-Saxon distribution for Pb^{208}

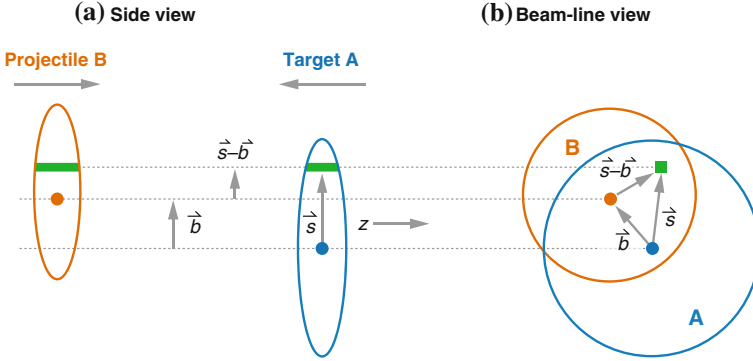


Fig. 2.21 Views of the collision system transverse (*left*) and parallel (*right*) to the beam axis [120]

Each nucleon in A can interact with a nucleon in B with probability $p_{AB} = \frac{T_{AB}\sigma_{NN}^{\text{inel}}}{AB}$, so the total probability of n collisions is binomial and is given by

$$P(n, \mathbf{b}) = \binom{n}{k} p_{AB}^n (1 - p_{AB})^{AB-n}. \quad (2.64)$$

This allows for the definition of the expected number of collisions as $N_{\text{coll}} = T_{AB}\sigma_{NN}^{\text{inel}}$, and the expected number of participants N_{part} , the total number of nucleons that participated in any scatterings (sometimes referred to as wounded nucleons) as

$$N_{\text{part}} = \int d^2b' T_A(\mathbf{b}') \left[1 - \left(1 - \frac{T_B(\mathbf{b}' - \mathbf{b})}{B} \right)^B \right] + \int d^2b' T_B(\mathbf{b}') \left[1 - \left(1 - \frac{T_A(\mathbf{b}' - \mathbf{b})}{A} \right)^A \right]. \quad (2.65)$$

An alternative to performing the analytic integrals is to use Monte Carlo techniques. This has the advantage of including terms neglected in the optical approximation that incorporate local per-event density fluctuations [120, 122]. This method is performed by sampling the full Woods-Saxon distribution in Eq. 2.61 A times to populate positions for nucleus A. To prevent overlap, a position is regenerated if it is found to be within some minimum distance of a previously generated nucleon. Once the positions have been generated for both nuclei, a random impact parameter vector is generated defining an offset between the nuclear centers. The transverse position for all nucleons in nucleus A is compared to each of the analogous nucleons in B. If the distance between the pair is $\Delta r < \sqrt{\sigma_{NN}^{\text{inel}}/\pi}$, the nucleons are considered to have participated. N_{coll} is defined as the number of times this condition is satisfied, with N_{part} defining the number of nucleons for which this condition was satisfied at

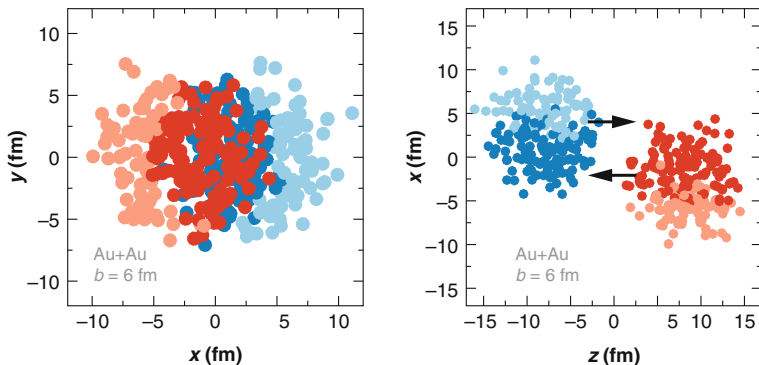


Fig. 2.22 Distributions of nucleons generated with the MC Glauber procedure in the x - y (left) and z - x (right) planes for Au¹⁹⁷. The two nuclei are shown in different colors, with the participants shown in a darker color [120]

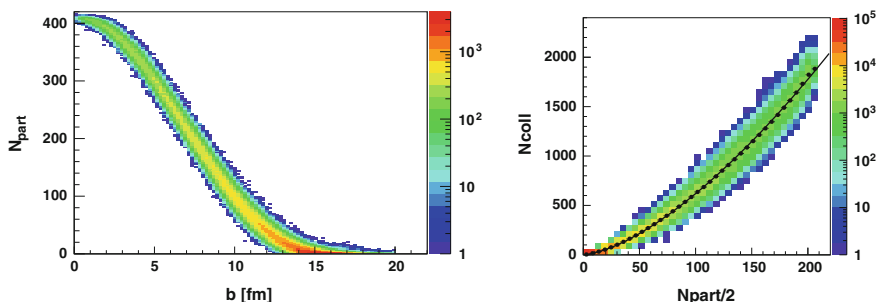
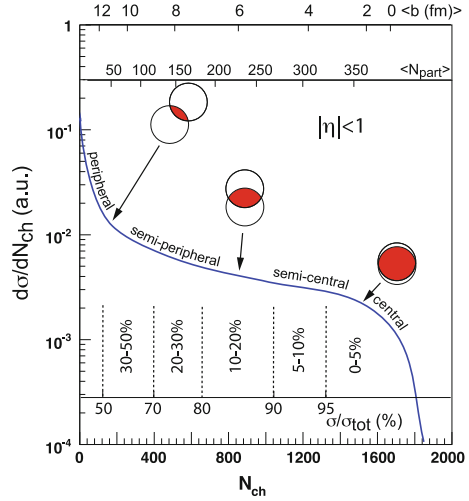


Fig. 2.23 Distribution of N_{part} values as a function of b (left) and the correlation between N_{part} and N_{coll} (right) for Pb+Pb collisions

least once. An example of an event generated with this technique is shown for an Au+Au collision in Fig. 2.22. The distribution of N_{part} values for different impact parameters is shown in Fig. 2.23, as well as the relationship between N_{coll} and N_{part} .

Experimentally, the per-event impact parameter is not measurable so a procedure must be performed to relate a distribution of some measurable quantity to the Glauber parameters. Variables like the total charged particle multiplicity or transverse energy typically have distributions similar to the N_{part} and N_{coll} distributions. This feature, combined with the fact that these are global variables and therefore less sensitive to detailed features and fluctuations make them excellent choices for centrality variables. The centrality determination procedure considers the minimum bias distribution of such a variable, ζ , and divides the range of observed values into sub-ranges where the integral of the distribution over that range is some percentage of the total; an example of this division is shown in Fig. 2.24. These sub-ranges are called centrality intervals, and centrality-dependent observables are usually calculated by averaging over all events in the same interval.

Fig. 2.24 Schematic diagram from Ref. [120] of a distribution of a centrality variable, in this case the number of charged particles in the interval $|\eta| < 1$. The events contributing to the upper 5 % of the integral of the distribution are the 0–5 % centrality bin, with near complete nuclear overlap. The parameters from a Glauber simulation, $\langle b \rangle$, $\langle N_{\text{part}} \rangle$, are shown as different *horizontal scales*



The i th centrality bin, $\zeta_i < \zeta < \zeta_{i+1}$, is typically defined in terms of percentages, a – b %, such that:

$$\int_{\zeta_{\min}}^{\zeta_i} d\zeta \frac{1}{N_{\text{evt}}} \frac{dN_{\text{evt}}}{d\zeta} = a \%, \quad \int_{\zeta_{i+1}}^{\zeta_{\max}} d\zeta \frac{1}{N_{\text{evt}}} \frac{dN_{\text{evt}}}{d\zeta} = b \%. \quad (2.66)$$

The Glauber model parameters must then be related to the class of events in a particular centrality bin. This can be accomplished by constructing a new variable, ξ , from the Glauber variables N_{coll} and N_{part} such that the ξ distribution is similar to the experimentally observed ζ distribution. The ζ distributions tend to be similar enough to the N_{coll} and N_{part} distributions that a simple linear combination of the two, a two-component model, is a suitable choice for ξ ,

$$\xi = \xi_0 \left(x \frac{N_{\text{part}}}{2} + (1 - x) N_{\text{coll}} \right). \quad (2.67)$$

The parameters ξ_0 and x can be determined from fitting the measured $dN_{\text{evt}}/d\zeta$ distribution with $dN_{\text{evt}}/d\xi$ from an MC Glauber sample. The centrality bins for ξ are defined in terms of integral fractions just as for ζ . In the i th centrality bin, the N_{coll} and N_{part} are averaged over all events for which $\xi_i < \xi < \xi_{i+1}$. These $\langle N_{\text{coll}} \rangle$ and $\langle N_{\text{part}} \rangle$ values are then associated with the i th centrality bin in the data.

2.5.2 Nuclear Modification

The first evidence for modification in nuclear collisions at high energy was observed $p+A$ collisions, where it was found that the production of particles at large transverse momentum ($2 \lesssim p_T \lesssim 6$ GeV) was enhanced in these collisions relative to pp [123, 124]. This effect, Cronin enhancement, was originally interpreted as additional transverse momentum, $k_t^2 \propto L$, imparted by additional, independent, elastic interactions with multiple nucleons. Here L is the average path length, which scales with atomic number as $L \propto A^{1/3}$.

The nuclear parton distribution functions (NPDFs), show both a suppression at lower values of x and an enhancement with increasing x with respect to the nucleon PDFs, termed shadowing and anti-shadowing respectively. This nuclear modification is quantified through the ratio,

$$R_i^A = \frac{f_i^A}{Af_i}, \quad (2.68)$$

where f are the PDFs for the nucleus A and the nucleon, and i is the parton species: valence quark, sea quark or gluon. When viewed in the rest frame of the target nucleus, the shadowing/anti-shadowing is the result of multiple scattering processes that destructively/constructively interfere at the amplitude level [125]. In the collinear factorized approach coherent multiple scattering terms are suppressed by powers of $1/Q^2$, however, for a large nucleus these contributions receive an enhancement of $A^{1/3}$, leading to sensitivity to higher twist effects [126].

When viewed in the infinite momentum frame, the shadowing effects arise from recombination of low- x gluons in the nuclear wave function [127]. This phenomenon is known as saturation and sets in as unitarity requirements force the nominal evolution equations to be modified at small x . The gluon distribution, $xG(x, Q^2)$, represents the number of gluons per unit rapidity in a region of transverse size $1/Q^2$ and grows as $\ln 1/x$ for small x at fixed Q^2 without this modification. However, as $Q^2 R^2 \lesssim xG(x, Q^2)$, where R is the radius of a nucleon, the gluons will begin to overlap and recombination of these gluons will limit the growth of $xG(x, Q^2)$ with decreasing x [128, 129].

At larger values of x , away from the shadowing/anti-shadowing region ($x \gtrsim 0.5$), the NPDFs exhibit additional suppression which is known as the EMC effect [130]. The origin of this effect may be related to non-nucleon degrees of freedom in the nucleus [131] and has led to increased interest in short-range correlations between nucleons. A sharp enhancement of the NPDF at the largest x values is thought to be described by the Fermi motion of the nucleons. Global analyses at NLO have been performed using data from DIS, Drell-Yan and $d+Au$ collisions at RHIC to extract the x -dependence of R_v^A , R_s^A and R_g^A at multiple Q^2 values [132]. These distributions, shown for Pb in Fig. 2.25, are a crucial input to any interpretation of any high- p_T phenomena observed in nucleus-nucleus collisions.

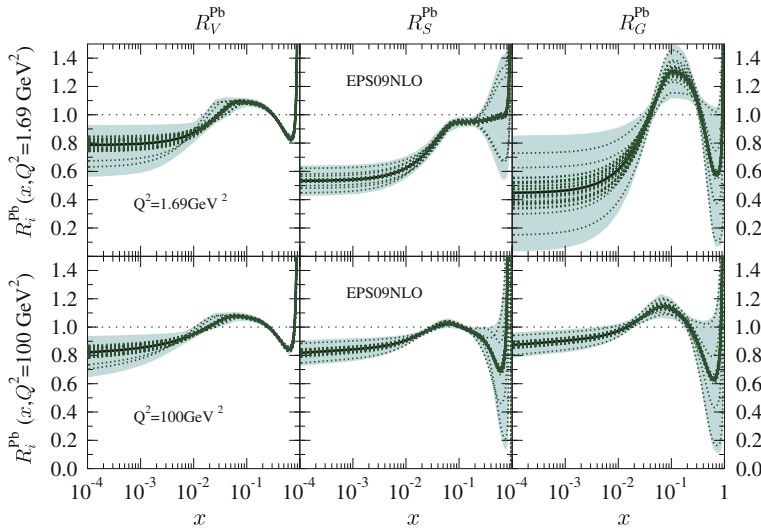


Fig. 2.25 Nuclear modification ratios R_V^{Pb} , R_S^{Pb} and R_G^{Pb} for the valence, sea and gluon PDFs for two values of Q^2 [132]. For Pb the shadowing region is $x \lesssim 0.05$, the anti-shadowing region is $0.05 \lesssim x \lesssim 0.5$ and the EMC region is $x \gtrsim 0.5$

2.5.3 HIJING

The phenomenology underlying the implementation of pp event generators such as PYTHIA, requires extensions to be appropriate for nucleus-nucleus collisions. An important step in achieving this was the development of the HIJING MC event generator [133]. To correctly model the multiplicity fluctuations the soft production mechanism combines elements of different models. It introduces multiple, sea $q\bar{q}$ strings as in the dual parton model [134–136], but also allows for induced gluon bremsstrahlung by introducing string kinks as in the Lund FRITIOF procedure [137, 138]. Additional transverse momentum kicks are applied that are dependent on the particle’s p_T proportional to $(p_T^2 + a^2)^{-1}(p_T^2 + p_0^2)^{-1}$.

The production of “minijets” with $p_T \geq p_0 \sim 2 \text{ GeV}$ is expected to play an important role in the total energy and particle production [139, 140]. These processes take place at an intermediate momentum scale, lower than that associated with typical jet production, but still describable by perturbative QCD. Production of multiple jets in HIJING is implemented through a probabilistic model of independent jet (pair) production. The average number of minijets at impact parameter b is given by $\sigma_{\text{jet}} T_N(b)$, where σ_{jet} is the inclusive cross section for jets in nucleon-nucleon collisions, integrated above some threshold p_0 . The probability for multiple independent minijet production is given by [141],

$$g_j(b) = \frac{(\sigma_{\text{jet}} T_N(b))^j}{j!} e^{-\sigma_{\text{jet}} T_N(b)}, \quad j \geq 1, \quad (2.69)$$

$$g_0(b) = \left[1 - e^{-\sigma_{\text{soft}} T_N(b)} \right] e^{-\sigma_{\text{jet}} T_N(b)}, \quad (2.70)$$

where σ_{soft} is the non-perturbative inclusive cross section for soft processes and $T_N(b)$ is the partonic overlap function between two nucleons separated by impact parameter b . An eikonal picture is used to relate the inelastic, elastic and total cross sections and to define the multi-jet probabilities for minijets in nucleon-nucleon collisions,

$$G_0 = \frac{\pi}{\sigma_{\text{in}}} \int_0^\infty d^2b \left[1 - e^{-2\chi_S(b,s)} \right] e^{-2\chi_H(b,s)} \quad (2.71)$$

$$G_j = \frac{\pi}{\sigma_{\text{in}}} \int_0^\infty d^2b \frac{[2\chi_H(b,s)]^j}{j!} e^{-2\chi_H(b,s)}. \quad (2.72)$$

Here the eikonal factors are related by $\chi_S + \chi_H = \chi_0(1 + \sigma_{\text{jet}}/\sigma_{\text{soft}})$, and ensure geometric scaling. The independence of the multi-jet production is an appropriate ansatz if $\sigma_{\text{jet}} \lesssim 2A^{-2/3}(p_0 R_N)^2 \sigma_{\text{inel}}$. The overall jet cross section is reduced from the nucleon-nucleon case to include the effects of nuclear shadowing, including the impact parameter dependence which has not been measured by experiment. The modification factor defined in Eq. 2.68 can be generalized to include impact parameter dependence,

$$R_A(x, Q^2, e) = R_A^0(x, Q^2) + \alpha(r) R_A^S(x, Q^2), \quad (2.73)$$

where $\alpha(r) \propto (A^{1/3} - 1) \sqrt{1 - r^2/R_A^2}$, models the impact parameter dependence [133]. Then the effective jet cross section is a function of the transverse positions of each of the colliding nucleons in the binary system,

$$\sigma_{\text{jet}}^{\text{eff}}(r_A, r_B) = \sigma_{\text{jet}}^0 + \alpha_A(r_A) \sigma_{\text{jet}}^A + \alpha_B(r_B) \sigma_{\text{jet}}^B + \alpha_A(r_A) \alpha_B(r_B) \sigma_{\text{jet}}^{\text{AB}}. \quad (2.74)$$

The event generation proceeds by using an MC Glauber setup to determine the set of colliding nucleon pairs. For each of these binary collisions, the probability of scattering and number of jets is determined, along with whether the collision is elastic or inelastic. Hard scattering partons are treated separately, and their energies are subtracted from the nucleons with the remaining energy used in processing soft string excitations. The resulting scattered gluons are ordered in rapidity and color-connected to the valence quark/di-quark of the nucleon. The correlated semi-hard particle production mechanism is the key feature of HIJING and is why it has remained a useful tool long after its inception.

2.5.4 Jet Quenching

A significant form of nuclear modification occurs in heavy ion collisions where the byproducts of hard scatterings can interact with the QGP through the phenomenon of jet quenching. The character of this interaction provides key insight into the dynamics of the medium. The most important is the identification of the relevant scales for the jet-medium interaction and whether it can be described by perturbative QCD. If so, it provides a key testing ground for thermal, perturbative QCD and the HTL formulation as well as an example of the transport phenomena of radiation and diffusion in a fundamental physical system.

The potential for jets as a tool to study the plasma was first recognized by Bjorken [142], who suggested that events with back-to-back jets would be sensitive to differential energy loss if the two partons had different in-medium path lengths. In extreme cases a highly energetic jet may emerge while its partner deposits all of its energy in the medium, which would represent a striking experimental signature.

The energy loss mechanism originally proposed by Bjorken was through elastic collisions with the medium constituents. This was originally given in Ref. [142] as,

$$\frac{dE}{dx} = C_R \pi \alpha_S^2 T^2 \left(1 + \frac{N_f}{6} \right) \ln \frac{4ET}{m_D^2}, \quad (2.75)$$

with more intricate forms of the term inside the logarithm due to improvements in the collision integral given in Refs. [143–145]. In a QCD plasma, the Debye screening mass, m_D , is given by,

$$m_D = \left(1 + \frac{1}{6} N_f \right) g^2 T^2. \quad (2.76)$$

Some of the first predictions of jet quenching signatures involve a modification of the dijet acoplanarity distribution in heavy ion collisions [146, 147]. These calculations were formulated in terms of the probability distribution for dijet pairs to have momentum imbalance K_η ,

$$\frac{dP}{dK_\eta} \equiv \frac{1}{\sigma_0(p_T)} \frac{1}{p_T} \frac{d\sigma}{d\phi}. \quad (2.77)$$

The acoplanarity was expected to show a temperature-dependent modification due to elastic collisions with the medium constituents. It was shown that similar effects could be produced through collisional energy loss in a hadronic resonance gas [148], and thus an observed modification would not prove the presence of a QGP phase.

Interactions with the medium can also induce radiative energy loss through the emission of bremsstrahlung gluons. In QED, energy loss for high energy electrons is typically in the Bethe-Heitler regime $\frac{dE}{dx} = -\frac{E}{L}$, where L is a characteristic length. Classically, the total energy loss per scattering is the integral of the bremsstrahlung spectrum

$$\Delta E = \int d\omega dk_{\parallel}^2 \omega \frac{dI}{d\omega dk_{\parallel}^2} \quad (2.78)$$

with multiple scatterings adding incoherently to give a total energy loss

$$\Delta E^{\text{tot}} = N \int d\omega dk_{\parallel}^2 \omega \frac{dI}{d\omega dk_{\parallel}^2}, \quad (2.79)$$

where $N = L/\lambda$ is the medium opacity and λ is the mean free path between scattering centers.

Most models use a formalism that treats the medium as a series of static scattering centers with the parton and radiated gluons with energies, E and ω respectively, traveling along eikonal trajectories. This is combined with the kinematic limits $q_{\perp} \ll \omega \ll E$, where q_{\perp} is the momentum transfer with the medium. This kinematic regime is referred to as the soft eikonal limit [149]. The radiation spectrum is typically derived by using the single gluon emission kernel as a Poisson probability for multi-gluon emission.

At high energies, significant interference occurs between the parton and quanta emitted at small angles. This results in a finite formation time for the radiation and suppresses this contribution relative to incoherent radiation, known as the LPM effect [150, 151] in QED. The QCD analog of this phenomenon has been proposed as an important feature of the quenching mechanism [152, 153] and was shown by BDMPs [154] and independently by Zakharov [155] to give an energy loss that grows quadratically with path length in the medium $\Delta E \propto L^2$.

As the interference suppresses the coherent radiation, the emission spectrum will be dominated by those quanta which have decohered. These are gluons which have acquired a phase, φ , of order unity [156, 157],

$$\varphi = \left\langle \frac{q_{\perp}^2 \Delta z}{2\omega} \right\rangle \sim \frac{\hat{q} L^2}{2\omega}, \quad (2.80)$$

and thus appear with a characteristic energy,

$$\omega_c \equiv \frac{1}{2} \hat{q} L^2. \quad (2.81)$$

Here the transport coefficient \hat{q} has been introduced, which in this picture represents the mean squared transverse momentum imparted to the parton per unit length, $\hat{q} = \langle q_{\perp}^2 \rangle / L$.

In this picture the energy loss is determined by soft multiple scattering. In the coherent limit the parton undergoes Brownian motion with a Gaussian elastic cross section $\propto \frac{1}{\hat{q} L} e^{-q_{\perp}^2 / \hat{q} L}$, and the scattering centers behave as a single source of radiation. The bremsstrahlung spectrum is given by

$$\omega \frac{dI}{d\omega} \simeq \frac{2\alpha_S C_R}{\pi} \begin{cases} \sqrt{\frac{\omega_c}{\omega}} & \omega < \omega_c \\ \frac{1}{12} \left(\frac{\omega_c}{\omega}\right)^2 & \omega > \omega_c \end{cases}, \quad (2.82)$$

which results in energy loss $\Delta E \sim \alpha_S \omega_c = \frac{1}{2} \alpha_S \hat{q} L^2$. The L^2 dependence is qualitatively different than both the Bethe-Heitler energy loss and the LPM effect in QED ($\omega \frac{dI}{d\omega} \sim \sqrt{\omega}$).

Other models frame the energy loss as an expansion in opacity. These models are not restricted to small momentum transfers, including the power-law tail in the scattering cross section, but the coherence effects of BDMPS-Z formulation must be enforced order-by-order in opacity. The GLV [158, 159] model is an example of this approach, which models the scattering centers as screened Yukawa potentials with screening length, μ . The gluon spectrum is constructed by integrating first over the longitudinal direction to enforce the LPM interference at a given order. The momentum transfer q_\perp is then averaged over giving the double-differential gluon distribution, $\omega \frac{dI}{d\omega dk_\perp^2}$. This can be analyzed to give information about the transverse pattern of radiation before integrating over k_\perp and ω to give the full energy loss.

The ASW formalism [157, 160] is a path integral formulation that can be applied to both the multiple soft scattering (MS) or single hard (SH) dominated scenarios. In the SH approximation the gluon distribution agrees exactly with the GLV formula to first order in opacity, however, the assumptions of the two models and ranges of integration differ, giving different results for the total energy loss. In the limit where these differences can be neglected (ignoring the kinematic constraints) the radiation spectrum is given by [157],

$$\omega \frac{dI}{d\omega} \simeq \frac{2\alpha_S C_R}{\pi} \frac{L}{\lambda} \begin{cases} \frac{\pi}{4} \frac{\bar{\omega}_c}{\omega} & \omega < \bar{\omega}_c \\ \ln \frac{\bar{\omega}_c}{\omega} & \omega > \bar{\omega}_c \end{cases}, \quad (2.83)$$

where $\bar{\omega}_c = \frac{1}{2} \mu^2 L$ is a characteristic frequency, different than the BDMPS-Z case. In the SH scenario, the radiation is dominated by $\omega > \bar{\omega}_c$, also different from BDMPS-Z. The total energy loss,

$$\Delta E \simeq \frac{2\alpha_S C_R}{\pi} \frac{L}{\lambda} \bar{\omega}_c \ln \frac{E}{\bar{\omega}_c}, \quad (2.84)$$

is enhanced by $\ln \frac{E}{\bar{\omega}_c}$ relative to the region $\omega < \bar{\omega}_c$. Despite the differences from BDMPS-Z, this limit also gives $\Delta E \simeq L^2$.

The ASW approach allows for the calculation of quenching weights, which give the probability for gluon splitting in the medium. With the assumption of an ordering principle in the virtualities of the fast parton, these weights can be combined with the vacuum DGLAP splitting functions. These modified splitting functions can be

used to define a medium-evolved fragmentation function [161] and can be used to calculate the effect of quenching on jet shape observables [162].

Some of the difficulties occurring in these analytic calculations can be alleviated by considering an MC approach. These typically supplement the generation of hard scattering processes used in generators by an additional step to include the quenching effects, and allow for the application of medium effects to the entire jet, not just the leading parton (democratic treatment) [163]. Generators like Q-PYTHIA [164], PQM [165, 166] and JEWEL [167], replace the vacuum parton showers implemented in PYTHIA with medium modified parton showers by altering the Sudakov form factors to include the quenching weights. The PYQUEN model imposes radiative energy loss of the BDMPS-Z type as well as collisional energy loss before applying vacuum fragmentation [168].

The approach that most directly incorporates the thermal of the system was developed by Arnold, Moore and Yaffe (AMY) [169–174]. This relaxes some of the assumptions used by other models, and includes thermal partons which are dynamical scattering centers. Furthermore, the requirement that the emitted gluons be softer than the initial parton energy ($\omega \ll E$) is not required. The energy loss occurs through elastic scatterings with differential collision rates of the form

$$\frac{d\bar{\Gamma}}{d^2q_{\perp}} = \frac{1}{2\pi^2} \frac{g^2 T m_D^2}{\mathbf{q}_{\perp}^2 (\mathbf{q}_{\perp}^2 + m_D^2)}. \quad (2.85)$$

Multiple soft interactions are resummed using the HTL techniques discussed in Sect. 2.4.3, leading to a differential emission rate for each parton species $\frac{d\Gamma}{dk}$. These are used to construct rate equations describing the evolution of the momentum distributions. This setup treats collisional and radiative energy loss in a consistent picture, but loses the distinction between radiated and thermal gluons. Additionally, finite length effects which result in finite formation times for the radiated gluons, are not included in the formalism.

Although these formulations differ on a number of features, they do have some key elements in common. The most important of these is the operating assumption of factorization between the production cross section, energy loss process and fragmentation. While there is no rigorous proof of factorization in heavy ion collisions, experimental evidence supports the interpretation that quenching is not an initial-state effect and that final-state interactions are partonic in nature [149]. In all of these models, the quenching mechanism is not applied to the radiated quanta, thus the calculation is limited to the energy loss of the leading parton, except in the MC implementations. Furthermore, emitted quanta themselves are radiation sources. Coherence effects between these sources establish the angular ordering in the vacuum parton shower and allow for the cancellation of infrared and collinear divergences. Such effects may play an important role in medium-induced parton showers as well [175].

It should also be noted that all models use repeated application of an inclusive single gluon emission kernel, extending to multiple emissions either inferring a Pois-

son distribution or using rate equations. However, this is not the same as applying the exclusive multi-gluon emission. Implementing this type of emission forces the parton kinematics to be updated or dynamical changes in the medium. Including these local effects as well as the global effects from the LPM-type interference poses a serious challenge [149].

There are also issues with these approaches relating to the treatment of large angle radiation. The BDPMS-Z formalism receives its dominant contribution from radiation that is outside the valid kinematical range of the approximation [176]. In ASW and GLV, the transverse distribution of emitted gluons is calculable. For energy loss, this distribution is integrated over k_t and the behavior at large angles is linked to how the kinematic constraints on the parton are enforced and the assumption of collinearity. It has been shown that the choice of maximum opening angle θ_{\max} can change the results appreciably, leading to at the least a large systematic error [149, 177]. The effects of different transverse cutoffs are shown in Fig. 2.26. The different physical pictures have made it difficult to consistently fix parameters for a direct comparison of models. However, a recent comparison was performed by applying the GLV, AMY and ASW (both MS and SH) formalisms to a “brick” of QGP matter of fixed length [149]. A comparison of medium-induced gluon emission spectra and nuclear suppression factors as a function of \hat{q} for each of the different models are shown in Figs. 2.27 and 2.28 respectively.

Depending on the formalism, the quenching mechanism is sensitive to the system size as well as some combination of the intensive parameters \hat{q} , μ and λ , which provide information about the microscopic medium dynamics. The soft multiple scattering approximation is only sensitive to \hat{q} , which is defined as the mean-squared momentum transfer per unit length,

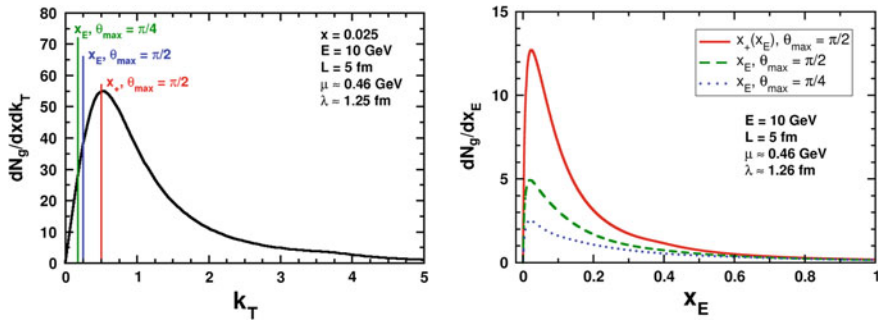


Fig. 2.26 The double differential gluon distribution (*left*), $\frac{dN}{dxdk_t}$, calculated in the GLV formalism at fixed x . Here, $x = \omega/E$, is the fraction of the quenched parton’s energy carried away by the radiated gluon. The effect of different kinematic cutoffs in the k_t integration is illustrated by the vertical lines. The effects of these cutoffs on the integration is shown on the *right*. Figures adapted from Ref. [149]

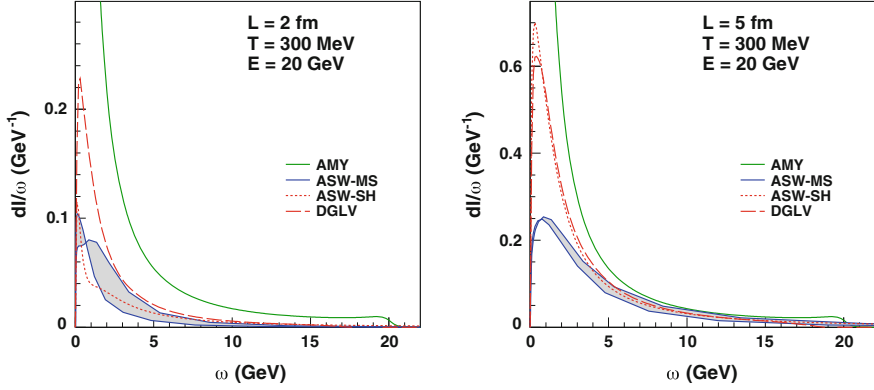


Fig. 2.27 Single gluon emission spectrum $\frac{dI}{d\omega}$ as a function of gluon energy ω for the AMY, GLV, ASW-MS and ASW-SH formalisms. The calculations are for a 20 GeV parton passing through QGP bricks at $T = 300$ MeV with size $L = 2$ fm and $L = 5$ fm, shown on the *left* and *right* respectively. Figure adapted from Ref. [149]

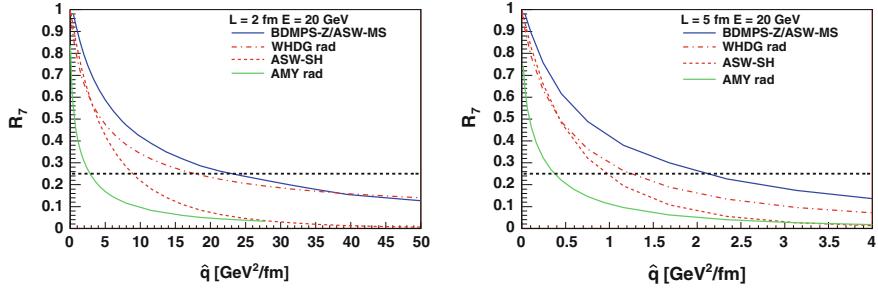


Fig. 2.28 Comparison between different models of the single hadron suppression factor, R_7 , of a p_T^{-7} spectrum as a function of \hat{q} respectively. Figure adapted from Ref. [149]

$$\hat{q} = \rho \int d^2 q_T q_T^2 \frac{d\sigma}{d^2 q_T} \equiv \int_0^{q_{\max}} d^2 q_{\perp} \mathbf{q}_{\perp}^2 \frac{d\Gamma_{\text{el}}}{d^2 q_{\perp}}, \quad (2.86)$$

where $\frac{d\Gamma_{\text{el}}}{d^2 q_{\perp}}$ is the differential elastic scattering rate for a hard parton in a thermal medium. This behaves as $\frac{1}{q_{\perp}^2}$ at high temperatures, but is screened at low temperatures by m_D^2 , given by Eq. 2.76. The form,

$$\frac{d\Gamma_{\text{el}}}{d^2 q_{\perp}} \simeq \frac{C_R}{(2\pi)^2} \frac{g^4 \mathcal{N}}{\mathbf{q}_{\perp}^2 (\mathbf{q}_{\perp}^2 + m_D^2)}, \quad (2.87)$$

interpolates smoothly between these limits [149], and the number density \mathcal{N} has been introduced [178],

$$\mathcal{N} = \frac{\zeta(3)}{\zeta(2)} \left(1 + \frac{1}{4}N_f\right) T^3. \quad (2.88)$$

The leading coefficient is the ratio of Riemann zeta function values, $\frac{\zeta(3)}{\zeta(2)} \approx 0.731$. The value of \hat{q} is given by,

$$\hat{q}(T) = \frac{C_R g^4 \mathcal{N}(T)}{4\pi} \ln \left(1 + \frac{q_{\max}^2(T)}{m_D^2(T)}\right), \quad (2.89)$$

where q_{\max}^2 is the largest transverse momentum transfer allowed in the elastic scatterings and is a function of T and in principle the parton energy as well. This introduces a logarithmic dependence of \hat{q} on E , which is an effect of approximating the collision integral in the evaluation of the elastic scattering rate. This value is sometimes taken as $q_{\max}^2 = g^2 ET$ although $q_{\max}^2 = g^2 \sqrt{ET^3}$ may be more appropriate [179]. The value,

$$\hat{q} \approx \frac{m_D^2}{\lambda} = \frac{C_R g^4 \mathcal{N}(T)}{4\pi} \propto T^3, \quad (2.90)$$

and λ calculated below, is a commonly used, energy independent expression and is equivalent to omitting the logarithmic variation of \hat{q} . These estimates can differ by up to 40 % for large parton energies.

The opacity can be calculated as

$$n = \frac{L}{\lambda} = L \int d^2 q_{\perp} \frac{d\Gamma_{\text{el}}}{d^2 q_{\perp}}, \quad (2.91)$$

which in turn, determines λ . However, the form of the scattering rate here is slightly different than the one given in Eq. 2.87, and is chosen to be consistent with the model used in the opacity expansion framework [149]. This gives

$$\lambda = \frac{4\pi m_D^2}{C_R g^4 \mathcal{N}}, \quad (2.92)$$

which is consistent with Eq. 2.90.

Motivated by new experimental capabilities at the LHC, extensions of energy loss calculations to full jets have recently been made [180–182]. These function by expressing the differential jet cross section as,

$$\frac{d\sigma_{\text{jet}}^{\text{AA}}}{dE_T dy} = \langle N_{\text{coll}} \rangle \sum_q \int dx P_q(x, E_T) \frac{d\sigma_q}{dE'_T dy} |\mathcal{J}_q(x)|, \quad (2.93)$$

where $P_q(x)$ is the probability a jet will lose a fraction x of its energy. The Jacobian $|\mathcal{J}(x)|$ relates the initial and final parton E_T by $E'_T = |\mathcal{J}_q(x)|E_T$, and is given by

$$|\mathcal{J}_q(x)| = \left[1 - x(1 - f_q(R, p_T^{\min})) \right]^{-1}. \quad (2.94)$$

The factor $f_q(R, p_T^{\min})$ is the fraction of the emitted radiation above p_T^{\min} and inside the jet cone defined by R ,

$$f_q(R, p_T^{\min}) = \frac{\int_0^R dr \int_{p_T^{\min}}^{E_T} d\omega \frac{dI_q}{d\omega dr}}{\int_0^\infty dr \int_0^{E_T} d\omega \frac{dI_q}{d\omega dr}}. \quad (2.95)$$

While this form still only considers the energy loss of the leading parton, it does take into account the extent to which radiated energy is not lost, but only redistributed within the jet. Furthermore, it facilitates the usage of NLO and NPDF effects in the pQCD calculation of the unmodified jet cross section, $\frac{d\sigma_q}{dE_T dy}$. The factorization of medium-induced radiation from the production cross section, which is used in Eq. 2.93 has been proven in the context of an effective theory. This uses Soft Collinear

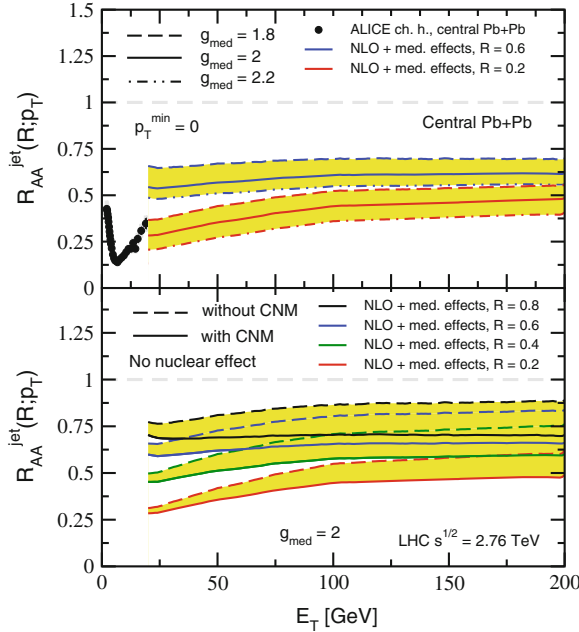


Fig. 2.29 Calculation of jet R_{AA} for various jet radii as a function of jet E_T (bottom). The top panel shows a comparison to single particle R_{AA} . Predictions with and without NPDF effects are shown in the solid and dashed lines. Figure adapted from Ref. [182]

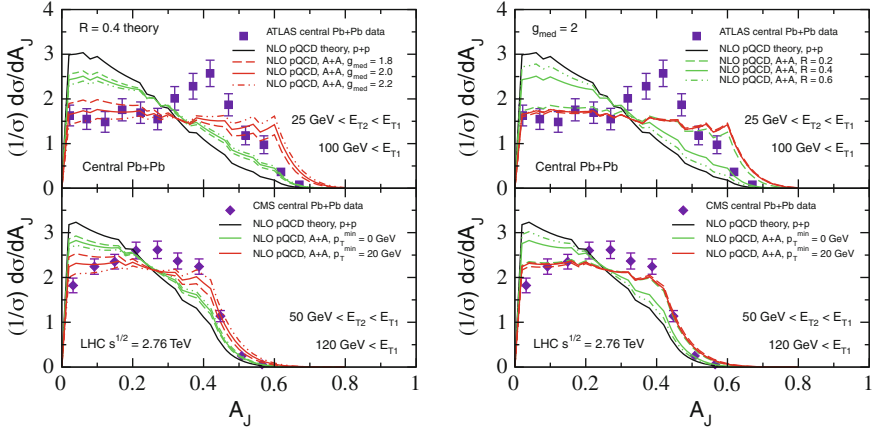


Fig. 2.30 Calculation of jet dijet asymmetry for various model parameters using kinematic cuts chosen to match measurements from ATLAS (*left*) and CMS (*right*). Figure adapted from Ref. [182]

Effective Theory (SCET) techniques to decouple the hard and soft components of the gluon fields and has been shown to reproduce the GLV expression when expanded to first order in opacity [183]. This factorization is also applicable to multi-jet systems, allowing calculations of differential energy loss in dijet systems. Calculations of the inclusive jet suppression factor and dijet asymmetry in this framework are shown in Figs. 2.29 and 2.30, respectively.

The AdS/CFT correspondence principle was discussed in Sect. 2.4.4, in the context of estimating the shear viscosity. Similar techniques have also been applied to study the energy loss of fast partons. While many of these results have focused on the specific case of heavy quarks [184–187], some work has been done to provide an estimate of \hat{q} [188–190]. These results agree qualitatively with the range of \hat{q} estimates from experiment.

2.6 Relativistic Heavy Ion Collisions: RHIC to LHC

With the commencement of the RHIC program, many of the speculated features of heavy ion collisions became experimentally accessible. The collective behavior of the system can be studied by measuring the angular distribution of particles, $\frac{dN}{d\phi}$. As discussed previously, in the absence of hydrodynamical expansion, this distribution is expected to be isotropic. The anisotropy can be quantified by considering the Fourier decomposition of the distribution,

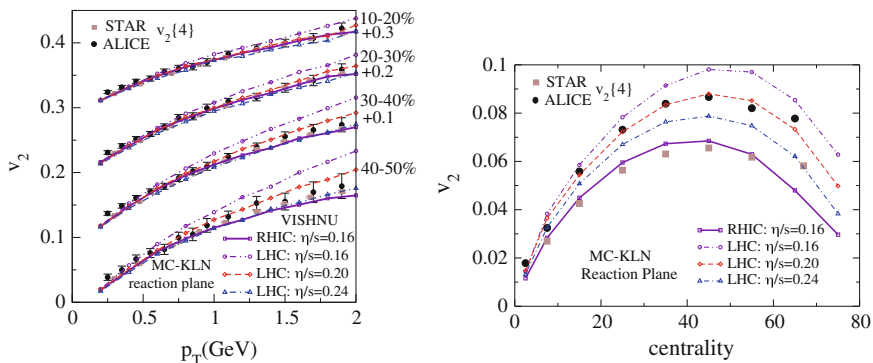


Fig. 2.31 Values of v_2 as a function of p_T (left) and centrality (right) measured by the STAR (Au+Au, $\sqrt{s_{NN}} = 200$ GeV) [191] and ALICE (Pb+Pb, $\sqrt{s_{NN}} = 2.76$ TeV) [192] collaborations are compared with values calculated from the VISHNU viscous hydro model with hadron cascade [193]. The elliptic flow is measured using a four-particle cumulant technique

$$\frac{dN}{d\phi} = f \left\{ 1 + \sum_{n=1}^{\infty} 2v_n \cos[n(\phi - \Psi_n)] \right\}, \quad (2.96)$$

where Ψ_n are the event plane angles, and v_n describe the magnitude of the modulation. In all but the most central collisions, the direction of the impact parameter vector between the nuclear centers defines a reaction plane. The overlap region is ellipsoidal and symmetric about this reaction plane. The second Fourier coefficient, v_2 , is an observable with sensitivity to how the initial-state anisotropy is converted to the final-state particle distribution, a phenomenon known as elliptic flow. Measurements from the RHIC program show that the elliptic flow, in particular the magnitude of the azimuthal modulation of particles as a function of their p_T , is well-described by ideal, relativistic hydrodynamics. The near-vanishing viscosity indicates that the system is strongly coupled. This came as a surprise when compared to the prediction of asymptotically free quarks and gluons and which has led to monikers such as the strongly-coupled QGP (sQGP) and “the perfect liquid” applied to the medium created at RHIC. Since early RHIC results, significant advances have been made in the formulation and numerical implementation of viscous hydrodynamics. RHIC and LHC v_2 values are compared with a recent viscous hydrodynamical calculation in Fig. 2.31.

More recently, it was recognized that the event-by-event fluctuations in collision geometry could drive higher flow harmonics. These provide additional information about the initial-state geometry and may be able to provide additional constraints on the hydrodynamical formulation or the value of the shear viscosity. The first six harmonics as measured by ATLAS [194] are shown in Fig. 2.32.

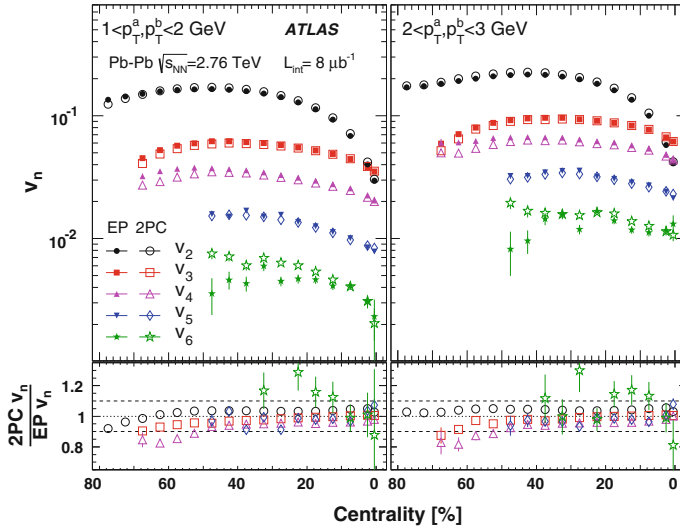


Fig. 2.32 Values of $v_1 - v_6$ as a function of centrality measured by ATLAS [194]. Two techniques, two-particle correlations (*open markers*) and the event plane method (*solid markers*), were used and were found to be in good agreement. The ratio of the results from the two methods is shown in the *bottom panel*

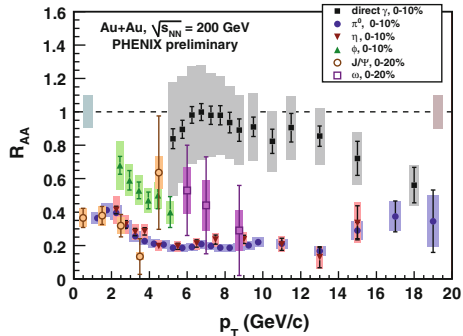
2.6.1 Hard Processes

Indirect experimental evidence for jet quenching was first established by two important measurements. The single hadron spectrum was found to be heavily suppressed at high- p_T in central collisions [195–198]. Furthermore, the away-side correlation in the dihadron angular distribution was found to be heavily modified in central Au + Au relative to pp [199, 200]. These two measurements provide slightly different handles on the phenomenon as the former is an inclusive measurement of the total effect of the suppression on the p_T spectrum. The latter provides a differential measurement of the quenching as it is sensitive to the quenching of one jet relative to another.

The interpretation of these observations as evidence for quenching was further supported by results from the d + Au run which established a critical baseline. The lack of suppression at high- p_T [201, 202] combined with the unmodified dihadron correlation indicated that modification of the NPDFs was not responsible for the observations in Au + Au. Subsequent measurements of the direct photon R_{AA} were consistent with no suppression and provided further systematic control on the quenching effects [203].

The degree of suppression is typically quantified by the nuclear modification factor, R_{AA} ,

Fig. 2.33 PHENIX R_{AA} measurements for π^0 , η , ϕ , ω , J/ψ and direct γ [204]



$$R_{AA} = \frac{E \frac{d^3 n_{\text{jet}}^{\text{cent}}}{dp^3}}{T_{AA} E \frac{d^3 \sigma_{\text{jet}}^{\text{p+p}}}{dp^3}}. \quad (2.97)$$

A summary of the R_{AA} measurements from PHENIX is shown in Fig. 2.33. These results established that the production of high- p_T particles is strongly influenced by the produced medium in heavy ion collisions. However, the single particle measurements (with the exception of the photon), are limited in their utility. The medium effects involve a high momentum parton, not a final-state hadron. Thus single particle observables can only be connected to the process of interest through a fragmentation function. This necessity forces the interpretation of the results in the context of strict factorization between the medium effects and fragmentation. While this factorization may ultimately prove to be an appropriate assumption, it is desirable and more objective to work in a more general paradigm for the jet-medium interaction, namely one that does not enforce strict separation between medium effects and the jet fragmentation. Furthermore, the single hadron observables are only linked to the parton level quantities in an average sense; there is no guarantee that the highest energy hadron in an event came from the leading jet, or the jet that suffered the least energy loss. This limitation is removed if per-jet fragmentation distribution is eliminated from the observable.

It is less restrictive, although more experimentally challenging, to construct observables from fully reconstructed jets. These quantities provide direct sensitivity to quenching effects. Furthermore, the possibility of using jets as input objects into physics analyses opens many new possibilities, which will be discussed in detail in Chap. 7. Measurements of full jets at RHIC have been attempted, but are limited by a number of factors and as of this time no such measurement has been published. The main complication is due to the production rates of jets that are easily detectable above the medium background. Measurements are further constrained by the limited acceptance of the PHENIX and STAR detectors. Although highly collimated, particles from jets can still be distributed over a substantial angular range. Typical sizes

for the cone radii and R parameters in the sequential clustering algorithms used in pp experiments are on the order of 0.5. Thus larger acceptance detectors are preferred for jet measurements.

Many of these issues are not present at the LHC, in particular the ATLAS experiment, discussed at length in Chap. 3. At these high energies, the first Pb+Pb run was at $\sigma_{NN} = 2.76$ TeV, the rate for producing jets well above the background from the underlying event is much higher; the differential single jet inclusive cross section $d\sigma/dE_T d\eta \sim 1$ nb for 100 GeV jets in pp collisions at these energies. Furthermore, the high quality calorimetry covering 10 units in η enables precise measurements of jets and their properties.

References

1. M. Han, Y. Nambu, Three triplet model with double $SU(3)$ symmetry. Phys. Rev. **139**, B1006–B1010 (1965)
2. M. Gell-Mann, Symmetries of baryons and mesons. Phys. Rev. **125**, 1067–1084 (1962)
3. M. Gell-Mann, A schematic model of Baryons and Mesons. Phys. Lett. **8**, 214–215 (1964)
4. J.J.J. Kokkedee, The quark model, CERN-TH-757 (1967)
5. G. Zweig, An SU_3 model for strong interaction symmetry and its breaking: Part I, CERN-TH-401 (1964)
6. G. Zweig, An SU_3 model for strong interaction symmetry and its breaking: Part II, CERN-TH-412 (1964)
7. V. Barnes et al., Observation of a hyperon with strangeness -3 . Phys. Rev. Lett. **12**, 204–206 (1964)
8. J. Bjorken, Asymptotic sum rules at infinite momentum. Phys. Rev. **179**, 1547–1553 (1969)
9. E.D. Bloom et al., High-energy inelastic ep scattering at 6-Degrees and 10-Degrees. Phys. Rev. Lett. **23**, 930–934 (1969)
10. J.I. Friedman, H.W. Kendall, Deep inelastic electron scattering. Ann. Rev. Nucl. Part. Sci. **22**, 203–254 (1972)
11. J. Bjorken, E.A. Paschos, Inelastic Electron-Proton and gamma-Proton scattering, and the structure of the Nucleon. Phys. Rev. **185**, 1975–1982 (1969)
12. R.P. Feynman, Very high-energy collisions of hadrons. Phys. Rev. Lett. **23**, 1415–1417 (1969)
13. R.P. Feynman, *The behavior of hadron collisions at extreme energies*. Invited paper at the Third Conference on High-Energy Collisions (Stony Brook, New York, Sep 1969), pp. 5–6
14. M. Gell-Mann, F. Low, Quantum electrodynamics at small distances. Phys. Rev. **95**, 1300–1312 (1954)
15. K.G. Wilson, Non-Lagrangian models of current algebra. Phys. Rev. **179**, 1499–1512 (1969)
16. C.G. Callan, Broken scale invariance in scalar field theory. Phys. Rev. D **2**, 1541–1547 (1970)
17. K. Symanzik, Small distance behavior in field theory and power counting. Commun. Math. Phys. **18**, 227–246 (1970)
18. C.G. Callan, D.J. Gross, Bjorken scaling in quantum field theory. Phys. Rev. D **8**, 4383–4394 (1973)
19. N.H. Christ, B. Hasslacher, A.H. Mueller, Light cone behavior of perturbation theory. Phys. Rev. D **6**, 3543 (1972)
20. C.-N. Yang, R.L. Mills, Conservation of isotopic spin and isotopic gauge invariance. Phys. Rev. **96**, 191–195 (1954)
21. H. Politzer, Reliable perturbative results for strong interactions? Phys. Rev. Lett. **30**, 1346–1349 (1973)

22. D. Gross, F. Wilczek, Ultraviolet behavior of non-abelian gauge theories. *Phys. Rev. Lett.* **30**, 1343–1346 (1973)
23. D. Gross, F. Wilczek, Asymptotically free gauge theories. 1. *Phys. Rev. D* **8**, 3633–3652 (1973)
24. D. Gross, F. Wilczek, Asymptotically free gauge theories. 2. *Phys. Rev. D* **9**, 980–993 (1974)
25. H. Politzer, Asymptotic freedom: an approach to strong interactions. *Phys. Rept.* **14**, 129–180 (1974)
26. H. Georgi, H. Politzer, Electroproduction scaling in an asymptotically free theory of strong interactions. *Phys. Rev. D* **9**, 416–420 (1974)
27. S. Drell, T. Yan, Massive Lepton pair production in Hadron-Hadron collisions at high-energies. *Phys. Rev. Lett.* **25**, 316–320 (1970)
28. CTEQ Collaboration, Handbook of perturbative QCD; version 1.1: Sept. 1994. *Rev. Mod. Phys.* (1994)
29. K. Nakamura et al., Review of particle physics. *J. Phys. G* **37**, 075021 (2010)
30. C.G. Callan, D.J. Gross, High-energy electroproduction and the constitution of the electric current. *Phys. Rev. Lett.* **22**, 156–159 (1969)
31. A. Bodek et al., Experimental studies of the Neutron and Proton electromagnetic structure functions. *Phys. Rev. D* **20**, 1471–1552 (1979)
32. V. Ezhela, S. Lugovsky, O. Zenin, Hadronic part of the muon $g-2$ estimated on the $\sigma_{\text{tot}}^{2003}(e^+e^- \rightarrow \text{hadrons})$ evaluated data compilation. arXiv:hep-ph/0312114
33. G. Hanson et al., Evidence for jet structure in hadron production by e^+e^- annihilation. *Phys. Rev. Lett.* **35**, 1609–1612 (1975)
34. S.L. Wu, e^+e^- Physics at PETRA: the first 5-years. *Phys. Rept.* **107**, 59–324 (1984)
35. S. Bethke, The 2009 world average of α_s . *Eur. Phys. J. C* **64**, 689–703 (2009). arXiv:0908.1135
36. L. Faddeev, V. Popov, Feynman diagrams for the Yang-Mills field. *Phys. Lett. B* **25**, 29–30 (1967)
37. G.F. Sterman, S. Weinberg, Jets from quantum chromodynamics. *Phys. Rev. Lett.* **39**, 1436 (1977)
38. Y.L. Dokshitzer, D. Diakonov, S. Troian, Hard processes in quantum chromodynamics. *Phys. Rept.* **58**, 269–395 (1980)
39. G.F. Sterman, Mass divergences in annihilation processes. 1. Origin and nature of divergences in cut vacuum polarization diagrams. *Phys. Rev. D* **17**, 2773 (1978)
40. K.G. Wilson, Confinement of quarks. *Phys. Rev. D* **10**, 2445–2459 (1974)
41. H.B. Nielsen, M. Ninomiya, Absence of neutrinos on a lattice. 1. Proof by homotopy theory. *Nucl. Phys.* **B185**, 20 (1981)
42. H.B. Nielsen, M. Ninomiya, No go theorem for regularizing chiral fermions. *Phys. Lett.* **B105**, 219 (1981)
43. J.B. Kogut, L. Susskind, Hamiltonian formulation of Wilson’s lattice gauge theories. *Phys. Rev.* **D11**, 395 (1975)
44. K. Symanzik, Continuum limit and improved action in lattice theories. 1. Principles and ϕ^4 theory. *Nucl. Phys.* **B226**, 187 (1983)
45. A. Bazavov et al., Nonperturbative QCD simulations with $2+1$ flavors of improved staggered quarks. *Rev. Mod. Phys.* **82**, 1349–1417 (2010). arXiv:0903.3598
46. Y. Nambu, Lectures at the copenhagen, symposium (1970)
47. T. Goto, Relativistic quantum mechanics of one-dimensional mechanical continuum and subsidiary condition of dual resonance model. *Prog. Theor. Phys.* **46**, 1560–1569 (1971)
48. B. Andersson et al., Parton fragmentation and string dynamics. *Phys. Rept.* **97**, 31–145 (1983)
49. T. Sjostrand, High-energy physics event generation with PYTHIA 5.7 and JETSET 7.4. *Comput. Phys. Commun.* **82**, 74–90 (1994)
50. J.C. Collins, D.E. Soper, G.F. Sterman, Factorization for short distance Hadron-Hadron scattering. *Nucl. Phys.* **B261**, 104 (1985)
51. J.C. Collins, D.E. Soper, G.F. Sterman, Soft gluons and factorization. *Nucl. Phys.* **B308**, 833 (1988)

52. J.C. Collins, D.E. Soper, G.F. Sterman, Factorization of hard processes in QCD. *Adv. Ser. Direct. High Energy Phys.* **5**, 1–91 (1988). arXiv:hep-ph/0409313
53. S.J. Brodsky, D.S. Hwang, I. Schmidt, Final-state interactions and single-spin asymmetries in semi-inclusive deep inelastic scattering. *Phys. Lett.* **B530**, 99–107 (2002). arXiv:hep-ph/0201296
54. S.J. Brodsky et al., Structure functions are not parton probabilities. *Phys. Rev. D* **65**, 114025 (2002). arXiv:hep-ph/0104291
55. J.C. Collins, Leading twist single transverse-spin asymmetries: Drell-Yan and deep inelastic scattering. *Phys. Lett. B* **536**, 43–48 (2002). arXiv:hep-ph/0204004
56. D. Boer, P. Mulders, F. Pijlman, Universality of T -odd effects in single spin and azimuthal asymmetries. *Nucl. Phys. B* **667**, 201–241 (2003). arXiv:hep-ph/0303034
57. J.C. Collins, D.E. Soper, Back-to-back jets in QCD. *Nucl. Phys. B* **193**, 381 (1981)
58. J.C. Collins, D.E. Soper, G.F. Sterman, Transverse momentum distribution in Drell-Yan Pair and W and Z Boson production. *Nucl. Phys. B* **250**, 199 (1985)
59. J. Collins, J.-W. Qiu, k_t factorization is violated in production of high-transverse-momentum particles in hadron-hadron collisions. *Phys. Rev. D* **75**, 114014 (2007). arXiv:0705.2141
60. T.C. Rogers, P.J. Mulders, No generalized transverse momentum dependent factorization in the hadroproduction of high transverse momentum hadrons. *Phys. Rev. D* **81**, 094006 (2010). arXiv:1001.2977
61. G. Altarelli, G. Parisi, Asymptotic Freedom in Parton Language. *Nucl. Phys. B* **126**, 298 (1977)
62. V. Gribov, L. Lipatov, Deep inelastic ep scattering in perturbation theory. *Sov. J. Nucl. Phys.* **15**, 438–450 (1972)
63. Y.L. Dokshitzer, Calculation of the structure functions for deep inelastic scattering and e^+e^- annihilation by perturbation theory in quantum chromodynamics. *Sov. Phys. JETP* **46**, 641–653 (1977)
64. A.H. Mueller, Multiplicity and Hadron distributions in QCD jets: nonleading terms. *Nucl. Phys. B* **B213**, 85 (1983)
65. Y.L. Dokshitzer, V.A. Khoze, S. Troian, Inclusive particle spectra from QCD cascades. *Int. J. Mod. Phys. A* **7**, 1875–1906 (1992)
66. Y.L. Dokshitzer, V.A. Khoze, A.H. Miller, S.I. Troyan, *Basics of perturbative QCD* (Basics of. Ed. Frontiers, Gif-sur-Yvette, 1991)
67. V.A. Khoze, W. Ochs, Perturbative QCD approach to multiparticle production. *Int. J. Mod. Phys. A* **12**, 2949–3120 (1997). arXiv:hep-ph/9701421
68. C. Fong, B. Webber, One and two particle distributions at small x in QCD jets. *Nucl. Phys.* **B355**, 54–81 (1991)
69. Y.L. Dokshitzer, V.S. Fadin, V.A. Khoze, Double logs of perturbative QCD for parton jets and soft Hadron spectra. *Z. Phys. C* **15**, 325 (1982)
70. D. de Florian, R. Sassot, M. Stratmann, Global analysis of fragmentation functions for protons and charged hadrons. *Phys. Rev. D* **76**, 074033 (2007). arXiv:0707.1506
71. D. de Florian, R. Sassot, M. Stratmann, Global analysis of fragmentation functions for pions and kaons and their uncertainties. *Phys. Rev. D* **75**, 114010 (2007). arXiv:hep-ph/0703242
72. M. Hirai, S. Kumano, T.-H. Nagai, K. Sudoh, Determination of fragmentation functions and their uncertainties. *Phys. Rev. D* **75**, 094009 (2007). arXiv:hep-ph/0702250
73. B. Webber, A QCD model for jet fragmentation including Soft Gluon interference. *Nucl. Phys.* **B238**, 492 (1984)
74. G. Marchesini et al., HERWIG: a Monte Carlo event generator for simulating hadron emission reactions with interfering gluons. Version 5.1. *Comput. Phys. Commun.* **67**, 465–508 (1992) (April 1991)
75. S. Catani et al., QCD matrix elements + parton showers, *JHEP* **0111** 063 (2001). arXiv:hep-ph/0109231
76. J. Alwall et al., Comparative study of various algorithms for the merging of parton showers and matrix elements in hadronic collisions. *Eur. Phys. J. C* **53**, 473–500 (2008). arXiv:0706.2569

77. T. Gleisberg et al., SHERPA 1. alpha: a proof of concept version. JHEP **0402**, 056. arXiv:hep-ph/0311263
78. M.L. Mangano, M. Moretti, F. Piccinini, R. Pittau, A.D. Polosa, ALPGEN, a generator for hard multiparton processes in hadronic collisions. JHEP **0307**, 001 (2003). arXiv:hep-ph/0206293
79. J.E. Huth et al., Toward a standardization of jet definitions, FERMILAB-CONF-90-249-E (1990)
80. S.D. Ellis, Z. Kunszt, D.E. Soper, The one jet inclusive cross-section at order α_s^3 quarks and gluons. Phys. Rev. Lett. **64**, 2121 (1990)
81. G.P. Salam, Towards jetography. Eur. Phys. J. C **67**, 637–686 (2010). arXiv:0906.1833
82. M. Cacciari, G.P. Salam, G. Soyez, The anti- k_t jet clustering algorithm. JHEP **0804**, 063 (2008). arXiv:0802.1189
83. JADE Collaboration, Experimental studies on multi-jet production in e^+e^- annihilation at PETRA energies. Z. Phys. C **33**, 23 (1986)
84. JADE Collaboration, Experimental investigation of the energy dependence of the strong coupling strength. Phys. Lett. B **213**, 235 (1988)
85. S. Catani et al., New clustering algorithm for multi-jet cross-sections in e^+e^- annihilation. Phys. Lett. B **269**, 432–438 (1991)
86. S. Catani et al., Longitudinally invariant k_t clustering algorithms for hadron hadron collisions. Nucl. Phys. B **406**, 187–224 (1993)
87. S.D. Ellis, D.E. Soper, Successive combination jet algorithm for hadron collisions. Phys. Rev. D **48**, 3160–3166 (1993). arXiv:hep-ph/9305266
88. M. Cacciari, G.P. Salam, Dispelling the N^3 myth for the k_t jet-finder. Phys. Lett. B **641**, 57–61 (2006). arXiv:hep-ph/0512210
89. Y.L. Dokshitzer et al., Better jet clustering algorithms, JHEP **9708**, 001 (1997). arXiv:hep-ph/9707323
90. M. Wobisch, T. Wengler, Hadronization corrections to jet cross-sections in deep inelastic scattering. arXiv:hep-ph/9907280
91. ATLAS Collaboration, Jet Reconstruction Performance. ATL-PHYS-PUB-2009-012 (2009). <http://cdsweb.cern.ch/record/1167330/>
92. T. Kluge, K. Rabbertz, M. Wobisch, FastNLO: Fast pQCD calculations for PDF fits. arXiv:hep-ph/0609285
93. E. Fermi, High-energy nuclear events. Prog. Theor. Phys. **5**, 570–583 (1950)
94. L. Landau, On the multiparticle production in high-energy collisions. Izv. Akad. Nauk Ser. Fiz. **17**, 51–64 (1953)
95. R. Hagedorn, Statistical thermodynamics of strong interactions at high-energies. Nuovo Cim. Suppl. **3**, 147–186 (1965)
96. J.C. Collins, M. Perry, Superdense matter: neutrons or asymptotically free quarks? Phys. Rev. Lett. **34**, 1353 (1975)
97. E.V. Shuryak, Quantum chromodynamics and the theory of superdense matter. Phys. Rept. **61**, 71–158 (1980)
98. E.V. Shuryak, Two scales and phase transitions in quantum chromodynamics. Phys. Lett. B **107**, 103 (1981)
99. M. LeBellac, *Thermal Field Theory* (Cambridge University Press, Cambridge, 1996)
100. J.-P. Blaizot, E. Iancu, The quark gluon plasma: collective dynamics and hard thermal loops. Phys. Rept. **359**, 355–528 (2002). arXiv:hep-ph/0101103
101. A. Bazavov et al., Equation of state and QCD transition at finite temperature. Phys. Rev. D **80**, 014504 (2009). arXiv:0903.4379
102. E. Braaten, R.D. Pisarski, Soft amplitudes in hot gauge theories: a general analysis. Nucl. Phys. B **337**, 569 (1990)
103. E. Braaten, R.D. Pisarski, Simple effective Lagrangian for hard thermal loops. Phys. Rev. D **45**, 1827–1830 (1992)
104. H.A. Weldon, Covariant calculations at finite temperature: the relativistic plasma. Phys. Rev. D **26**, 1394 (1982)

105. A.D. Linde, Infrared problem in thermodynamics of the Yang-Mills Gas. *Phys. Lett. B* **96**, 289 (1980)
106. D.J. Gross, R.D. Pisarski, L.G. Yaffe, QCD and instantons at finite temperature. *Rev. Mod. Phys.* **53**, 43 (1981)
107. T. Lee, G. Wick, Vacuum stability and vacuum excitation in a spin 0 field theory. *Phys. Rev. D* **9**, 2291 (1974)
108. T.D. Lee, Abnormal nuclear states and vacuum excitations. *Rev. Mod. Phys.* **47**, 267 (1975)
109. K. Rajagopal, F. Wilczek, The condensed matter physics of QCD. [arXiv:hep-ph/0011333](#)
110. J. Bjorken, Highly relativistic nucleus-nucleus collisions: the central rapidity region. *Phys. Rev. D* **27**, 140–151 (1983)
111. PHENIX Collaboration, Measurement of the mid-rapidity transverse energy distribution from $\sqrt{s_{NN}} = 130$ GeV Au+Au collisions at RHIC. *Phys. Rev. Lett.* **87**, 052301 (2001). [arXiv:nucl-ex/0104015](#)
112. J.M. Maldacena, The large N limit of superconformal field theories and supergravity. *Adv. Theor. Math. Phys.* **2**, 231–252 (1998). [arXiv:hep-th/9711200](#)
113. O. Aharony et al., Large N field theories, string theory and gravity. *Phys. Rept.* **323**, 183–386 (2000). [arXiv:hep-th/9905111](#)
114. P. Danielewicz, M. Gyulassy, Dissipative phenomena in quark gluon plasmas. *Phys. Rev. D* **31**, 53–62 (1985)
115. G. Policastro, D. Son, A. Starinets, The shear viscosity of strongly coupled $N = 4$ supersymmetric Yang-Mills plasma. *Phys. Rev. Lett.* **87**, 081601 (2001). [arXiv:hep-th/0104066](#)
116. P. Kovtun, D.T. Son, A.O. Starinets, Holography and hydrodynamics: diffusion on stretched horizons. *JHEP* **0310**, 064 (2003). [arXiv:hep-th/0309213](#)
117. R.J. Glauber, in *Lectures in Theoretical Physics*, ed. by W.E. Brittin, L.G. Dunham, vol. 1 (Interscience, New York, 1959), pp. 315
118. R. Glauber, G. Matthiae, High-energy scattering of protons by nuclei. *Nucl. Phys. B* **21**, 135–157 (1970)
119. W. Czyz, L. Maximon, High-energy, small angle elastic scattering of strongly interacting composite particles. *Annals Phys.* **52**, 59–121 (1969)
120. M.L. Miller et al., Glauber modeling in high energy nuclear collisions. *Ann. Rev. Nucl. Part. Sci.* **57**, 205–243 (2007). [arXiv:nucl-ex/0701025](#)
121. H. De Vries, C.W. De Jager, C. De Vries, Nuclear charge and magnetization density distribution parameters from elastic electron scattering. *Atom. Data Nucl. Data Tabl.* **36**, 495–536 (1987)
122. A. Bialas, M. Bleszynski, W. Czyz, Multiplicity distributions in nucleus-nucleus collisions at high-energies. *Nucl. Phys. B* **111**, 461 (1976)
123. J. Cronin et al., Production of Hadrons with large transverse momentum at 200 GeV, 300 GeV, and 400 GeV. *Phys. Rev. D* **11**, 3105 (1975)
124. D. Antreasyan et al., Production of hadrons at large transverse momentum in 200 GeV, 300 GeV and 400 GeV pp and p+n collisions. *Phys. Rev. D* **19**, 764–778 (1979)
125. J.W. Qiu, I. Vitev, Coherent QCD multiple scattering in proton-nucleus collisions. *Phys. Lett. B* **632**, 507–511 (2006). [arXiv:hep-ph/0405068](#)
126. J.W. Qiu, G.F. Sterman, QCD and rescattering in nuclear targets. *Int. J. Mod. Phys. E* **12**, 149 (2003). [arXiv:hep-ph/0111002](#)
127. A.H. Mueller, J.W. Qiu, Gluon recombination and shadowing at small values of x . *Nucl. Phys. B* **268**, 427 (1986)
128. L. Gribov, E. Levin, M. Ryskin, Singlet structure function at small x : unitarization of gluon ladders. *Nucl. Phys. B* **188**, 555–576 (1981)
129. L. Gribov, E. Levin, M. Ryskin, Semihard processes in QCD. *Phys. Rept.* **100**, 1–150 (1983)
130. D.F. Geesaman, K. Saito, A.W. Thomas, The nuclear EMC effect. *Ann. Rev. Nucl. Part. Sci.* **45**, 337–390 (1995)
131. L. Frankfurt, M. Strikman, Hard nuclear processes and microscopic nuclear structure. *Phys. Rept.* **160**, 235–427 (1988)

132. K. Eskola, H. Paukkunen, C. Salgado, EPS09: a new generation of NLO and LO nuclear parton distribution functions. *JHEP* **0904**, 065 (2009). arXiv:0902.4154
133. X.N. Wang, M. Gyulassy, HIJING: a Monte Carlo model for multiple jet production in p p, p A and A A collisions. *Phys. Rev. D* **44**, 3501–3516 (1991)
134. A. Capella et al., Dual parton model. *Phys. Rept.* **236**, 225–329 (1994)
135. J. Ranft, Hadron production in hadron-nucleus and nucleus-nucleus collisions in the dual Monte Carlo multichain fragmentation model. *Phys. Rev. D* **37**, 1842 (1988)
136. J. Ranft, Transverse energy distributions in nucleus-nucleus collisions in the dual Monte Carlo multichain fragmentation model. *Phys. Lett. B* **188**, 379 (1987)
137. B. Andersson, G. Gustafson, B. Nilsson-Almqvist, A model for low p_T hadronic reactions, with generalizations to hadron-nucleus and nucleus-nucleus collisions. *Nucl. Phys. B* **281**, 289 (1987)
138. B. Nilsson-Almqvist, E. Stenlund, Interactions between hadrons and nuclei: the Lund Monte Carlo, Fritiof Version 1.6. *Comput. Phys. Commun.* **43**, 387 (1987)
139. K. Kajantie, P. Landshoff, J. Lindfors, Minijet production in high-energy nucleus-nucleus collisions. *Phys. Rev. Lett.* **59**, 2527 (1987)
140. K. Eskola, K. Kajantie, J. Lindfors, Quark and gluon production in high-energy nucleus-nucleus collisions. *Nucl. Phys. B* **323**, 37 (1989)
141. X.N. Wang, Role of multiple mini-jets in high-energy hadronic reactions. *Phys. Rev. D* **43**, 104–112 (1991)
142. J.D. Bjorken, fermilab-PUB-82/059-THY (1982)
143. M.H. Thoma, M. Gyulassy, Quark damping and energy loss in the high temperature QCD. *Nucl. Phys. B* **351**, 491–506 (1991)
144. E. Braaten, M.H. Thoma, Energy loss of a heavy quark in the quark-gluon plasma. *Phys. Rev. D* **44**, 2625–2630 (1991)
145. M.H. Thoma, Collisional energy loss of high-energy jets in the quark gluon plasma. *Phys. Lett. B* **273**, 128–132 (1991)
146. D.A. Appel, Jets as a probe of quark-gluon plasmas. *Phys. Rev. D* **33**, 717 (1986)
147. J. Blaizot, L.D. McLerran, Jets in expanding quark-gluon plasmas. *Phys. Rev. D* **34**, 2739 (1986)
148. M. Rammerstorfer, U.W. Heinz, Jet acoplanarity as a quark-gluon plasma probe. *Phys. Rev. D* **41**, 306–309 (1990)
149. N. Armesto et al., Comparison of jet quenching formalisms for a Quark-Gluon plasma ‘Brick’. arXiv:1106.1106
150. L. Landau, I. Pomeranchuk, Limits of applicability of the theory of bremsstrahlung electrons and pair production at high-energies. *Dokl. Akad. Nauk Ser. Fiz.* **92**, 535–536 (1953)
151. A.B. Migdal, Bremsstrahlung and pair production in condensed media at high-energies. *Phys. Rev.* **103**, 1811–1820 (1956)
152. M. Gyulassy, M. Plumer, Jet quenching in dense matter. *Phys. Lett. B* **243**, 432–438 (1990)
153. M. Gyulassy, X.N. Wang, Multiple collisions and induced gluon bremsstrahlung in QCD. *Nucl. Phys. B* **420**, 583–614 (1994). arXiv:nucl-th/9306003
154. R. Baier, Y.L. Dokshitzer, A.H. Mueller, S. Peigne, D. Schiff, Radiative energy loss of high-energy quarks and gluons in a finite volume quark-gluon plasma. *Nucl. Phys. B* **483**, 291–320 (1997). arXiv:hep-ph/9607355
155. B. Zakharov, Fully quantum treatment of the Landau-Pomeranchuk-Migdal effect in QED and QCD. *JETP Lett.* **63**, 952–957 (1996). arXiv:hep-ph/9607440
156. R. Baier, Jet quenching. *Nucl. Phys. A* **715**, 209–218 (2003). arXiv:hep-ph/0209038
157. C.A. Salgado, U.A. Wiedemann, Calculating quenching weights. *Phys. Rev. D* **68**, 014008 (2003). arXiv:hep-ph/0302184
158. M. Gyulassy, P. Levai, I. Vitev, Jet quenching in thin quark gluon plasmas. 1. Formalism. *Nucl. Phys. B* **571**, 197–233 (2000). arXiv:hep-ph/9907461
159. M. Gyulassy, P. Levai, I. Vitev, Reaction operator approach to non-Abelian energy loss. *Nucl. Phys. B* **594**, 371–419 (2001). arXiv:nucl-th/0006010

160. U.A. Wiedemann, Transverse dynamics of hard partons in nuclear media and the QCD dipole. Nucl. Phys. B **582**, 409–450 (2000). arXiv:hep-ph/0003021
161. N. Armesto et al., Medium-evolved fragmentation functions. JHEP **0802**, 048 (2008). arXiv:0710.3073
162. A.D. Polosa, C.A. Salgado, Jet shapes in opaque media. Phys. Rev. C **75**, 041901 (2007). arXiv:hep-ph/0607295
163. K.C. Zapp, U.A. Wiedemann, Coherent radiative parton energy loss beyond the BDMPS-Z Limit. arXiv:1202.1192
164. N. Armesto, L. Cunqueiro, C.A. Salgado, Q-PYTHIA: a medium-modified implementation of final state radiation. Eur. Phys. J. C **63**, 679–690 (2009). arXiv:0907.1014
165. A. Dainese, C. Loizides, G. Paic, Leading-particle suppression in high energy nucleus-nucleus collisions. Eur. Phys. J. C **38**, 461–474 (2005). arXiv:hep-ph/0406201
166. C. Loizides, High transverse momentum suppression and surface effects in Cu+Cu and Au+Au collisions within the PQM model. Eur. Phys. J. C **49**, 339–345 (2007). arXiv:hep-ph/0608133
167. K. Zapp et al., A Monte Carlo Model for ‘Jet Quenching’. Eur. Phys. J. C **60**, 617–632 (2009). arXiv:0804.3568
168. I. Lokhtin, A. Snigirev, A model of jet quenching in ultrarelativistic heavy ion collisions and high-p(T) hadron spectra at RHIC. Eur. Phys. J. C **45**, 211–217 (2006). arXiv:hep-ph/0506189
169. P.B. Arnold, G. D. Moore, and L. G. Yaffe, Transport coefficients in high temperature gauge theories. 1. Leading log results. JHEP **0011**, 001 (2000). arXiv:hep-ph/0010177
170. P.B. Arnold, G.D. Moore, L.G. Yaffe, Photon emission from ultrarelativistic plasmas. JHEP **0111**, 057 (2001). arXiv:hep-ph/0109064
171. P.B. Arnold, G.D. Moore, L.G. Yaffe, Photon emission from quark gluon plasma: complete leading order results. JHEP **0112**, 009 (2001). arXiv:hep-ph/0111107
172. P.B. Arnold, G.D. Moore, L.G. Yaffe, Photon and gluon emission in relativistic plasmas. JHEP **0206**, 030 (2002). arXiv:hep-ph/0204343
173. S. Jeon, G.D. Moore, Energy loss of leading partons in a thermal QCD medium. Phys. Rev. C **71**, 034901 (2005). arXiv:hep-ph/0309332
174. S. Turbide, C. Gale, S. Jeon, G.D. Moore, Energy loss of leading hadrons and direct photon production in evolving quark-gluon plasma, Phys. Rev. C **72**, 014906 (2005). arXiv:hep-ph/0502248
175. Y. Mehtar-Tani, C.A. Salgado, K. Tywoniuk, Anti-angular ordering of gluon radiation in QCD media. Phys. Rev. Lett. **106**, 122002 (2011). arXiv:1009.2965
176. U.A. Wiedemann, Jet quenching versus jet enhancement: a quantitative study of the BDMPS-Z gluon radiation spectrum. Nucl. Phys. A **690**, 731–751 (2001). arXiv:hep-ph/0008241
177. W. Horowitz, B. Cole, Systematic theoretical uncertainties in jet quenching due to gluon kinematics. Phys. Rev. C **81**, 024909 (2010). arXiv:0910.1823
178. P.B. Arnold, W. Xiao, High-energy jet quenching in weakly-coupled quark-gluon plasmas. Phys. Rev. D **78**, 125008 (2008). arXiv:0810.1026
179. S. Caron-Huot, O(g) plasma effects in jet quenching. Phys. Rev. D **79**, 065039 (2009). arXiv:0811.1603
180. I. Vitev, S. Wicks, B.W. Zhang, A theory of jet shapes and cross sections: from hadrons to nuclei. JHEP **0811**, 093 (2008). arXiv:0810.2807
181. I. Vitev, B.W. Zhang, Jet tomography of high-energy nucleus-nucleus collisions at next-to-leading order. Phys. Rev. Lett. **104**, 132001 (2010). arXiv:0910.1090
182. Y. He, I. Vitev, B.W. Zhang, Next-to-leading order analysis of inclusive jet and di-jet production in heavy ion reactions at the Large Hadron Collider (2012). arXiv:1105.2566
183. G. Ovanessian, I. Vitev, An effective theory for jet propagation in dense QCD matter: jet broadening and medium-induced bremsstrahlung. JHEP **1106**, 080 (2011). arXiv:1103.1074
184. S.S. Gubser, Drag force in AdS/CFT. Phys. Rev. D **74**, 126005 (2006). arXiv:hep-th/0605182
185. C. Herzog, A. Karch, P. Kovtun, C. Kozcaz, L. Yaffe, Energy loss of a heavy quark moving through $N = 4$ supersymmetric Yang-Mills plasma. JHEP **0607**, 013 (2006). arXiv:hep-th/0605158

186. J. Casalderrey-Solana, D. Teaney, Heavy quark diffusion in strongly coupled $N = 4$ Yang-Mills. *Phys. Rev. D* **74**, 085012 (2006). arXiv:hep-ph/0605199
187. J. Casalderrey-Solana, D. Teaney, Transverse momentum broadening of a fast quark in a $N = 4$ Yang Mills Plasma. *JHEP* **0704**, 039 (2007). arXiv:hep-th/0701123
188. H. Liu, K. Rajagopal, U.A. Wiedemann, Calculating the jet quenching parameter from AdS/CFT. *Phys. Rev. Lett.* **97**, 182301 (2006). arXiv:hep-ph/0605178
189. H. Liu, K. Rajagopal, U.A. Wiedemann, Wilson loops in heavy ion collisions and their calculation in AdS/CFT. *JHEP* **0703**, 066 (2007). arXiv:hep-ph/0612168
190. N. Armesto, J.D. Edelstein, J. Mas, Jet quenching at finite 't Hooft coupling and chemical potential from AdS/CFT. *JHEP* **0609**, 039 (2006). arXiv:hep-ph/0606245
191. STAR Collaboration, Centrality dependence of charged hadron and strange hadron elliptic flow from $\sqrt{s_{NN}} = 200$ GeV Au+Au collisions. *Phys. Rev. C* **77**, 054901 (2008). arXiv:0801.3466
192. ALICE Collaboration, Elliptic flow of charged particles in Pb+Pb collisions at 2.76 TeV. *Phys. Rev. Lett.* **105**, 252302 (2010). arXiv:1011.3914
193. H. Song, S.A. Bass, U. Heinz, Elliptic flow in 200 A GeV Au+Au collisions and 2.76 A TeV Pb+Pb collisions: insights from viscous hydrodynamics + hadron cascade hybrid model. *Phys. Rev. C* **83**, 054912 (2011). arXiv:1103.2380
194. ATLAS Collaboration, Measurement of the azimuthal anisotropy for charged particle production in $\sqrt{s_{NN}} = 2.76$ TeV lead-lead collisions with the ATLAS detector. *Phys. Rev. C* (2012) . arXiv:1203.3087.
195. PHENIX Collaboration, Suppression of hadrons with large transverse momentum in central Au+Au collisions at $\sqrt{s_{NN}} = 130$ GeV. *Phys. Rev. Lett.* **88**, 022301 (2002). arXiv:nucl-ex/0109003
196. PHENIX Collaboration, Suppressed π^0 production at large transverse momentum in central Au+Au collisions at $\sqrt{s_{NN}} = 200$ GeV. *Phys. Rev. Lett.* **91**, 072301 (2003). arXiv:nucl-ex/0304022
197. STAR Collaboration, Centrality dependence of high p_T hadron suppression in Au+Au collisions at $\sqrt{s_{NN}} = 130$ GeV. *Phys. Rev. Lett.* **89**, 202301 (2002). arXiv:nucl-ex/0206011
198. STAR Collaboration, Transverse momentum and collision energy dependence of high p_T hadron suppression in Au+Au collisions at ultrarelativistic energies. *Phys. Rev. Lett.* **91**, 172302 (2003). arXiv:nucl-ex/0305015
199. STAR Collaboration, Disappearance of back-to-back high p_T hadron correlations in central Au+Au collisions at $\sqrt{s_{NN}} = 200$ GeV. *Phys. Rev. Lett.* **90**, 082302 (2003). arXiv:nucl-ex/0210033
200. STAR Collaboration, Distributions of charged hadrons associated with high transverse momentum particles in pp and Au+Au collisions at $\sqrt{s_{NN}} = 200$ GeV. *Phys. Rev. Lett.* **95** 152301 (2005). arXiv:nucl-ex/0501016
201. PHENIX Collaboration, Absence of suppression in particle production at large transverse momentum in $\sqrt{s_{NN}} = 200$ GeV d+Au collisions. *Phys. Rev. Lett.* **91**, 072303 (2003). arXiv:nucl-ex/0306021
202. STAR Collaboration, Evidence from d+Au measurements for final state suppression of high p_T hadrons in Au+Au collisions at RHIC. *Phys. Rev. Lett.* **91**, 072304 (2003). arXiv:nucl-ex/0306024
203. PHENIX Collaboration, Centrality dependence of direct photon production in $\sqrt{s_{NN}} = 200$ GeV Au+Au collisions. *Phys. Rev. Lett.* **94**, 232301 (2005). arXiv:nucl-ex/0503003
204. K. Reygers, Characteristics of Parton Energy Loss Studied with High- p_T Particle Spectra from PHENIX. *J. Phys. G G* **35**, 104045 (2008). arXiv:0804.4562

<http://www.springer.com/978-3-319-01218-6>

Jet Quenching in Relativistic Heavy Ion Collisions at the
LHC

Angerami, A.

2014, XV, 169 p. 133 illus., 117 illus. in color.,

Hardcover

ISBN: 978-3-319-01218-6